FINITE ELEMENT MODELING, COMPUTER SIMULATIONS, AND EXPERIMENTS OF SHEAR WAVE PROPAGATION FOR TISSUE MECHANICAL PROPERTY ASSESSMENT

By
Allison Pinosky

Senior Honors Thesis
Department of Biomedical Engineering
University of North Carolina at Chapel Hill

2015

Approved:

____

Caterina Gallippi, Thesis Advisor

Devin Hubbard, Reader

Gianmarco Pinton, Reader

ABSTRACT

Allison Pinosky: Finite Element Modeling, Computer Simulations, and Experiments of Shear Wave Propagation for Tissue Mechanical Property Assessment
(Under the direction of Caterina Gallippi)

The goal of this project is to develop a novel approach to tissue mechanical property measurement using Acoustic Radiation Force Ultrasound. This project aims to do so by incorporating the quantitative nature of shear wave imaging with the minimal lateral displacement requirement of acoustic radiation force impulse imaging to develop a novel approach to tissue mechanical property measurement using statistical signal separation techniques. By applying a wide tracking beam to a narrow push, it hypothesized that principal component analysis may be used to reconstruct the shear wave and get tissue mechanical property information. This new approach will not require spatial averaging, as alternative methods do, and will therefore better reflect the mechanical properties of heterogeneous tissues.

To Mom, Dad, and Seth, thank you for all of your support.

ACKNOWLEDGEMENTS

First and foremost, I would like to thank Dr. Gallippi for the opportunity to conduct research in her lab and complete this honors thesis. I would also like to thank Tomek Czernuszewicz for all the time you spent helping me with this project and teaching me about ultrasound. This project was supported by the Sarah Steele Danhoff Undergraduate Research Fund administered by Honors Carolina.

TABLE OF CONTENTS

LIST OF TABLES viii

LIST OF FIGURES ix

LIST OF ABBREVIATIONS x

LIST OF SYMBOLS xi

CHAPTER 1: INTRODUCTION TO ULTRASOUND 2

- Ultrasound Elastography 2
- Acoustic Radiation Force (ARF) 3
- ARF Shear Wave Velocity Measurement 4
- Current Methods for Measuring Elasticity 5
- Benefits of Alternative Approach 7

CHAPTER 2: BLIND SOURCE SEPARATION (BSS) 8

CHAPTER 3: METHODS 10

- Finite Element Method (FEM) Simulation of Tissue Displacement 10
- Simulation of Ultrasonic Displacement Tracking 11
- Principal Component Analysis (PCA) Processing of Tracked Data 12

CHAPTER 4: RESULTS 14

- Finite Element Model (FEM) Mesh 14
- Kernels 15

Velocity Computation 20

CHAPTER 5: CONCLUSION & FUTURE DIRECTION 27

APPENDIX 1: SUPPLEMENTARY MATLAB FIGURES FOR ENTIRE DATA SET 29

APPENDIX 2: SUPPLEMENTARY MATLAB FIGURES FOR KERNELS 32

1λ Figures 32

1.5λ Figures 34

3λ Figures 37

Time-to-Peak (TTP) 39

Time-to-Recovery (TTR) 40

REFERENCES 42

LIST OF TABLES

Table 1: Expected Shear Wave Velocities for Simulated Young's Modulus Values ... 21

Table 2: Experimental Shear Wave Velocities for Simulated Young's Modulus Values Using Time Between Double Peaks as Change in Time for F/5 ... 22

Table 3: Expected and Experimental Shear Wave Velocities Ratios and Percent Error for Double Peaks ... 23

Table 4: Experimental Shear Wave Velocities for Simulated Young's Modulus Values Using Time-to-Recovery (TTR) as Change in Time ... 25

Table 5: Expected and Experimental Shear Wave Velocities Ratios and Percent Error for TTR (Excluding 50kPa) ... 26

LIST OF FIGURES

Figure 1: Ultrasound Transducer Configuration Properties and Intensity Field Transmission 2

Figure 2: Wave Propagation in Tissue 5

Figure 3: ARF Elasticity Imaging Methods 6

Figure 4: FEM Mesh with Quarter Symmetry Loaded with F/0.75 Push in LS-DYNA PrePost (left) and in MATLAB (right) 14

Figure 5: FEM Generated Mesh with Entire F/0.75 Point Spread 15

Figure 6: 10 Seeds and Mean Displacement Estimation for Eig. 1 of Entire Data Set 16

Figure 7: 10 Seeds and Mean Displacement Estimation for Eig. 2 of Entire Data Set 16

Figure 8: Mean Displacement Estimation with Standard Deviation for Eig. 1 of Entire Data Set 17

Figure 9: Selected Axial Kernels on F/0.75 Quarter Symmetry Mesh 18

Figure 10: Mean Displacement Estimation for Eig.1 of Three Kernels focused at 20mm Compared to Eig.1 of the Entire Data Set 18

Figure 11: Mean Displacement Estimation (Eig.1) Comparison to Mean Displacement Tracking for 1λ Focused at 20mm 20

Figure 12: Double Peak Detection for 1λ, Eig.1, at 20.03mm 22

Figure 13: Time-to-Peak (TTP) Detection for 1λ, Eig.1, at 20.03mm 24

Figure 14: Time-to-Recovery (TTR) Detection for 1λ, Eig.1, at 20.03mm 25

LIST OF ABBREVIATIONS

ARF	Acoustic Radiation Force
BSS	Blind Source Separation
FEM	Finite Element Method
ICA	Independent Component Analysis
PCA	Principal Component Analysis
RF	Radio-Frequency
ROE	Region of Excitation
SNR	Signal-to-Noise Ratio
TOF	Time-of-Flight
TTP	Time-to-Peak
TTR	Time-to-Recovery

LIST OF SYMBOLS

α	Tissue Attenuation Coefficient
c	Speed of Sound
c_t	Shear Wave Propagation Speed
D	Active Aperture Width
E	Young’s Modulus
$F/\#$	Focal Configuration, F-Number
f_S	Sampling Frequency
f_{TX}	Transmit Frequency
I	Local Temporal Average Intensity
λ	Wavelength
μ	Shear Modulus
ρ	Density
v	Poisson Ratio
z	Acoustic Focal Depth

CHAPTER 1: INTRODUCTION TO ULTRASOUND

Ultrasound imaging uses the transmission of sound and the reception of reflective sound to construct an image. This is possible because sound is a waveform whose speed depends on the medium through which it is traveling. Ultrasound provides a non-invasive means of examining tissue. To observe tissues, sound is transmitted directly into the body using a transducer. The transducer is capable of both transmitting and receiving acoustic waveforms.

Transducers are made with a variety of geometries and are designed with specific center frequencies and bandwidths. The transducer of interest for this application is a one-dimensional (1D) linear array. Linear array transducers are comprised of a single line of elements and have a fixed elevational focus (Palmeri, McAleavey, Trahey, & Nightingale, 200s6; Szabo, 2014). Selectively activating elements of this array, allows the creation of narrow or wide beam apertures. The number of active elements is determined by the beam width and the desired focal depth. The focal configuration constant, f-number (F/#) is calculated based on the acoustic focal depth (z) and the active aperture length (D):

$$F/\# = \frac{z}{D}$$

(Palmeri, Wang, Dahl, Frinkley, & Nightengale, 2009). Figure 1 illustrates these parameters.

Figure 1: Ultrasound Transducer Configuration Properties and Intensity Field Transmission

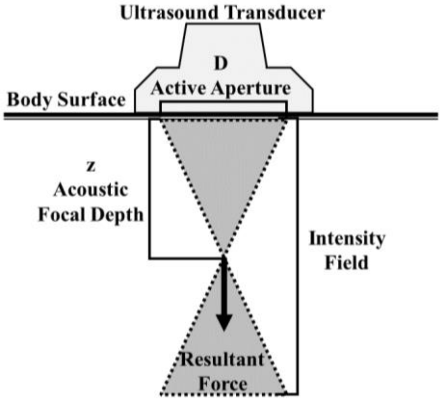

The transducer may transmit and receive waveforms in several different modes: A-mode, B-mode, M-mode, and Doppler. For this application, B-mode ultrasound imaging is used. B-mode produces a 2D, brightness-modulated image in which depth is along the z-axis (Szabo, 2014). Conventional B-mode imaging is able to distinguish features with different acoustic properties (Doherty, Trahey, Nightingale, & Palmeri, 2013). Image resolution depends on focal configuration (F/#), center frequency, and bandwidth (Szabo, 2014).

Ultrasound Elastography

In addition to ultrasound's imaging capabilities, it may be used to exert a force. This capability is utilized in an application called ultrasound elastography. Ultrasound elastography measures tissue displacement and recovery in response to external compression or vibration of tissue (Palmeri et al., 2006). By tracking tissue displacement and recovery over time, information regarding tissue stiffness may be extracted.

Detecting stiffer or more fibrotic tissue is desirable because tissue health has long been correlated to tissue stiffness, particularly in soft tissues. Although B-mode ultrasound imaging may be used to examine tissue, it is often difficult to distinguish stiff tissue from soft tissue because these masses grow out of the same tissue matrix (Szabo, 2014). A routine method of detecting superficial stiff regions is used to detect cancerous legions in breast tissue. By manually pressing on the superficial tissue, it is possible to physically feel discontinuities in the tissue (Doherty et al., 2013). These discontinuities, or stiff regions, may constitute cancerous legions. This manual palpation procedure may be replicated at locations deeper in the tissue via ultrasound elastography.

To understand how ultrasound elastography works in tissue, a base understanding of material elasticity must be established. Material elasticity describes the tendency of the material to deform in response to an applied force (Doherty et al., 2013). Material stiffness may described by Young's modulus. Young's modulus (E) may be calculated in terms of shear wave modulus (μ) and Poisson Ratio (v):

$$E = \mu * 2(1 + v) \,.$$

Shear modulus describes a material's resistance to shear while Poisson's ratio describes the deformation that occurs orthogonal to the material (Doherty et al., 2013).

Acoustic Radiation Force (ARF)

One method of conducting ultrasound elastography is by exciting the tissue with acoustic radiation force (ARF) (Palmeri et al., 2006). ARF employs a multi-cycle ultrasonic pulse that generates a force in the propagation medium using a single transducer. The force applied by conventional ultrasound imaging is not substantial enough to produce measureable displacements (Doherty et al., 2013). To create tissue displacements in the range of 1 to 10μm, peak ARF magnitudes are typically on the order of dynes (Doherty et al., 2013). The magnitude of localized compression in response to ARF is inversely correlated to the underlying stiffness (Nightingale, 2012). Therefore, softer tissues will displace further than stiff tissues.

ARF induces the propagation of acoustic waves through dissipative medium (Fahey, Nightingale, Nelson, Palmeri, & Trahey, 2005). In soft tissue, the majority of attenuation of an acoustic wave is due to absorption. The radiation force applied to tissue at any given spatial location may be calculated in terms of tissue attenuation coefficient (α), local temporal average intensity (*I*), and the speed of sound in tissue (c):

$$F = \frac{2\propto I}{c},$$

(Mazza, Nava, Hahnloser, Jochum, & Bajka, 2007; Nightingale, 2012). The resultant radiation force is localized in the center of the intensity field laterally and at the acoustic focal point axially. The shape of the intensity field, depicted in Figure 1, is dependent upon *F/#* (Palmeri et al., 2009).

Initially, tissue displacement response to the ARF is restricted to the region of excitation (ROE), with the peak displacements occurring near the acoustic focal location. Standard B-mode pulses may be used to monitor the movement of tissue under force. Behavior of the tissue following the initial excitation will be addressed in the following section.

ARF Shear Wave Velocity Measurement

After the initial tissue displacement, waves propagate away from the region of excitation (ROE). There are two primary types of waves which propagate in soft tissues: longitudinal and shear waves. Figure 2 displays how particles move differently with the propagation of each of these waves. Longitudinal waves cause particles to oscillate in the same direction that the wave is propagating while shear waves cause the particles to oscillate transversely to wave propagation (Doherty et al., 2013). Both longitudinal and shear waves may be described in terms of elastic moduli.

Figure 2: Wave Propagation in Tissue

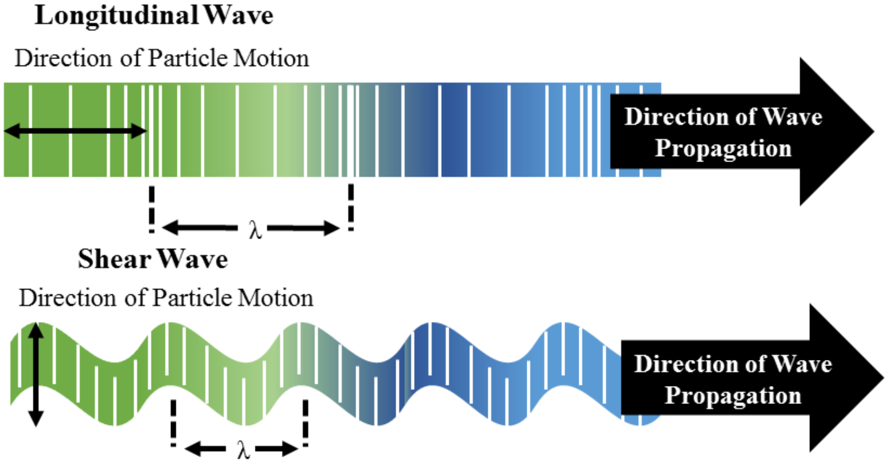

(Figure adapted from Olympus Corporation, n.d.)

In response to the ARF impulse, shear waves propagate radially away from the ROE. Tissue stiffness may then be inferred by measuring the velocity of the propagating shear wave. A faster shear wave velocity indicates propagation through stiffer tissue. This shear wave velocity (c_t), may be described in terms of shear modulus (μ) and in terms of tissue density (ρ):

$$c_t = \sqrt{\frac{\mu}{\rho}}$$

(Nightingale, 2012). Because shear modulus may be described in terms of Young's Modulus (E), shear wave velocity may be directly related to the Young's modulus of the tissue without requiring information about the force magnitude:

$$c_t = \sqrt{\frac{E}{2(1+v)\rho}}.$$

Current Methods for Measuring Elasticity

ARF methods are classified by the type of excitation pulse applied and the position of the tracking beams relative to the region of excitation (ROE). One excitation method, discussed herein, applies pulses—pushes—transiently in an impulse-like fashion (Doherty et al., 2013).

The tracking beam can then be placed on-axis (within the ROE) or off-axis (outside the ROE). Generally, on-axis methods can only provide relative, qualitative measures of elasticity while off-axis methods provide quantitative estimates (Doherty et al., 2013).

On-axis tracking may be performed using Acoustic Radiation Force Impulse (ARFI) imaging. ARFI excites and tracks tissue response from a single location (Figure 3). Then, the active aperture on the transducer is shifted over by one element, and the push and track sequence is repeated (Doherty et al., 2013). This process is repeated laterally across the field of view. The ARF induced compression is tracked with by B-mode pulses, which are used to detect the displacement of tissue and observe the recovery rate to the original state. ARFI images taken represent mechanical properties of the tissue rather than the acoustic properties. Axial displacements can then be calculated with normalized cross-correlation methods or phase-shift algorithms (Doherty et al., 2013). ARF allows relativistic detection of structural components but is unable to quantify the stiffness of structures absolutely because the true magnitude of the displacing force is unknown.

Figure 3: ARF Elasticity Imaging Methods

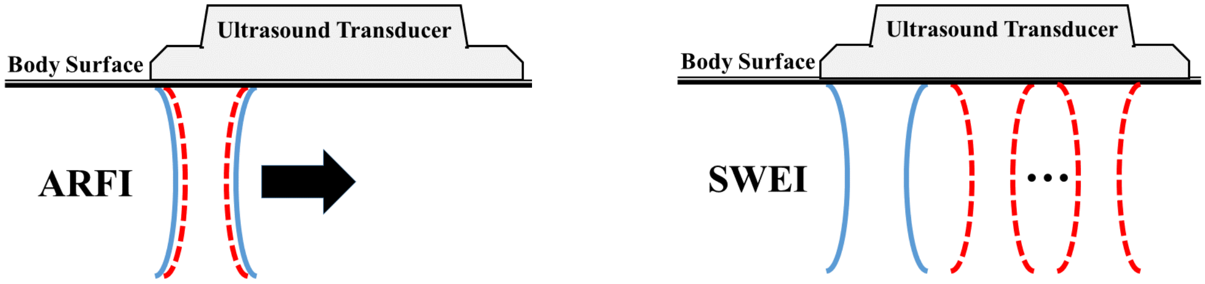

(Figure adapted from Doherty et al., 2013)

Off-axis tracking may be performed with Shear Wave Elasticity Imaging (SWEI). SWEI is an ARF method that tracks induced shear waves that radiate outward from the region of excitation. For SWEI, a push is emitted at one location and then the shear wave is tracked at multiple off-axis lateral locations at known distances from the initial push, as may be seen in

Figure 3 (Doherty et al., 2013). With SWEI, shear wave propagation can be characterized using time-of-flight (TOF) measurements. TOF measurements examine shear wave position as a function of time using time to peak displacement data outside the ROE (Palmeri et al., 2009). TOF methods make three assumptions: 1) the region adjacent to the ROE is homogeneous, 2) shear wave propagation is exclusively in the lateral direction, and 3) dispersion over the region is negligible (Palmeri et al., 2009). An advantage of shear wave imaging is that shear wave velocity measurements are force-independent and, therefore, quantitative.

Benefits of Alternative Approach

In this project, the aim is to incorporate the quantitative nature of shear wave imaging with the minimal lateral displacement requirement of ARF imaging to develop a novel approach to tissue mechanical property measurement using statistical signal separation techniques. This new approach will not require spatial averaging, as alternative methods do, and will therefore better reflect the mechanical properties of heterogeneous tissues.

CHAPTER 2: BLIND SOURCE SEPARATION (BSS)

Shear wave imaging may be improved by utilizing statistical signal separation techniques, such as a regression filter. Regression filters assume that signals are summations of polynomials in the time domain (Gallippi, Nightingale, & Trahey, 2003). Blind source separation (BSS) is a regression filter that additionally assumes statistical relationships exist between sources. BSS decomposes an original data matrix into displacement profile and noise source signal components (Gallippi et al., 2003).

Two approaches to BSS are principal component analysis (PCA) and independent component analysis (ICA). PCA assumes the source signals are orthogonal and Gaussian-distributed. PCA operates by organizing the data into orthogonal basis functions by corresponding energetic signatures (Gallippi et al., 2003). PCA is limited because orthogonality of basis functions does not necessarily imply that the functions are statistically independent, only that they are uncorrelated (Gallippi et al., 2003). If the functions are not Gaussian or otherwise distributed randomly, the basis functions may not be mutually independent. An alternate approach, ICA, assumes that the source signals are mutually independent in addition to being uncorrelated (Gallippi et al., 2003). ICA may preferable if the underlying source signals are statistically independent and non-Gaussian. For this application, PCA was selected as the desired BSS method.

PCA performs eigenvalue decomposition on a single matrix of data (X). If desired, a subset of the data may be selected for a specified kernel size (X_{KER}). To prepare the data for PCA, the desired matrix–whole or subset–is then transformed into complex data using the

Hilbert transform (X_H). This transformation is necessary because the purpose of performing PCA in this application is to attempt to isolate the shear wave propagating through the medium. Using complex data allows the decomposition to encode directional information.

Prior to eigenvalue decomposition, the data must be mean centered. This is accomplished by taking the mean of the data at each time point and subtracting that value from each element in the vector for the respective time point, resulting in a mean-centered matrix (X_{MC}). For an $[MxN]$ matrix X_H, where the N-dimension is the time-dimension, the following equation may be used to mean center the data:

$$X_{MC} = \begin{bmatrix} x_{1,1} - \overline{x_1} & \cdots & x_{1,N} - \overline{x_N} \\ \vdots & \ddots & \vdots \\ x_{M,1} - \overline{x_1} & \cdots & x_{M,N} - \overline{x_N} \end{bmatrix}$$

where $\overline{x_n}$ is the mean of respective columns n = 1…N and $x_{i,n}$ represent each element of the Hilbert transformed matrix (X_H) for i = 1…M. Next, the covariance matrix is computed and normalized:

$$X_{COV} = \frac{X_{MC}' * X_{MC}}{N-1}$$

where X_{MC} is the mean-centered, Hilbert transformed $[MxN]$ matrix and N is the number of time points.

Once the covariance matrix is computed, it can be decomposed into orthogonal eigenvalues and eigenvectors. BSS derived basis functions describe the contribution of the source signals that they span over time of ensemble acquisition (Gallippi et al., 2003). The eigenvalues with the larger values correspond to more energetic signals.

CHAPTER 3: METHODS

The aim of this project is to develop a method of separating ARFI data using BSS to allow shear wave tracking over a smaller area than is currently possible. The hope is that this will reduce inaccuracies due to special averaging. It is hypothesized that in order for BSS to be able to successfully separate out a shear wave velocity, a large tracking beam width, relative to a smaller tracking aperture, must be used.

Finite Element Method (FEM) Simulation of Tissue Displacement

Finite Element Method (FEM) is a mathematical way of finding approximate solutions to complex numerical problems for partial differential equations. For this project, an FEM model was developed to simulate radiation force-induced shear waves with a tight focal configuration (F/0.75) in a linearly elastic model. Simulated phantoms are uniform in geometry but differ by Young’s Modulus values (5kPa, 10kPa, 20kPa, 30kPa, and 50kPa).

The first phantom generation step establishes phantom geometry. The phantoms are simulated using LS-DYNA’s sub-program LS-PrePost (LS-DYNA, Livermore Software Technology Corporation, Livermore, CA). This program develops phantoms by generating a mesh. For each phantom, the fineness of the mesh and the distance in the elevational (x), lateral (y), and axial (z) directions may be specified. The finer the mesh, the more locations at which forces may be loaded and calculations performed. The tradeoff is that calculations for finer meshes take significantly longer to complete. To reduce the time required, phantoms may be constructed with quarter symmetry. For these simulations, a finely spaced phantom with quarter symmetry was constructed with dimensions of 10mm x 10mm x 40mm.

The second step, performed in MATLAB (MathWorks Inc., Natick, MA), establishes boundary conditions and initial conditions. The boundary conditions establish fully constrained top and bottom edges of the phantom. All edges of the phantom were specified to be non-reflecting to prevent the shear waves from bouncing back into the phantom. Next, FIELD II[1], a MATLAB-based linear acoustic field simulation tool, was used to load the F/0.75 Acoustic Radiation Force (ARF) ultrasound impulse onto the phantom. The program was used to simulate a Gaussian impulse at an excitation frequency of 4.21 MHz for a commercial linear array (VF7-3, Siemens Medical Solutions USA, Inc., Issaquah, WA). The push was focused in the center of the phantom at a depth of 20mm axially with a pulse duration of 400μs.

The third step prepares the material properties of the phantom. The phantom should be homogeneous and behave elastically with Poisson Ratio (v) of 0.499 and density (ρ) of 1 g/m^3. The simulation is set to run for 5ms, recording measurements every 10kHz. LS-DYNA is used to solve the dynamic equations of motion for tissue displacement. Displacement data is compiled for each simulation. This entire process must be repeated for each desired Young's Modulus value (5kPa, 10kPa, 20kPa, 30kPa, 50kPa).

Simulation of Ultrasonic Displacement Tracking

The second step in this project is performed in a MATLAB. FIELD II is used to simulate ultrasound transducer fields and ultrasound imaging from the collected FEM displacement data. The ultrasound transducer fields (scatterer realizations) generated by FIELD II are then used to generate unique raw ultrasound simulated signals (RF data) to represent scatterer displacements

---

[1] FIELD II is available for download at http://field-ii.dk/

in tissue. This process is performed for several variations of tracking aperture widths (F/0.75, F/1.5, F/3.0 and F/5.0).

Typically, the program determines the number of scatterers required based on the F/# for that specific simulation. To attain comparable results across different F/#'s, the scatterer number per resolution cell can be set to a uniform value for all simulations. This constraint is acceptable because it is only necessary for there to be at least 11 scatterers per resolution cell to ensure fully developed speckle. Furthermore, uniform scatterer number will ensure a signal-to-noise ratio (SNR) in the desired range. Approximately 1.2 million scatterers are used for these simulations, ensuring sufficient SNR. By re-running FIELD II for different scatterer realizations (seeds), multiple trials of RF data may be compiled for each stiffness and F/#.

Principal Component Analysis (PCA) Processing of Tracked Data

The third step in this project performs Principal Component Analysis (PCA) on the FIELD II simulated RF data. To perform PCA, all simulated RF data—for the desired scatterer realization, F/#, and Young's Modulus value—is loaded into a single matrix. Then, subsets of the data are selected using a specific kernel sizes. Kernel sizes are selected based on the sampling frequency (f_s), 200MHz, and wavelength (λ) of the RF data. The wavelength may be calculated from the speed of sound in tissue (c) and the transmission frequency (f_{TX}), 6.15MHz:

$$\lambda = \frac{c}{f_{TX}}.$$

Similarly, the displacement per sample (*DispPerSample*) may be calculated from the speed of sound in tissue (c) and the sampling frequency (f_S):

$$DispPerSample = \frac{c}{2 * f_S}.$$

The displacement per sample must be divided by two to account for the time it takes for the acoustic wave to travel into the tissue and reflect back. The number of samples required for the kernel (S_{KER}) can then be found for the desired portion of the wavelength (KER):

$$S_{KER} = \frac{KER * \lambda}{DispPerSample}.$$

Note, that subsequent discussions of subsets will define them in terms of wavelength in the form #λ. The desired matrix–whole or subset–is then transformed into complex data using the Hilbert transform.

Once the Hilbert transform is performed, the data mean centered, and the covariance matrix is computed. Then, the covariance matrix is decomposed into eigenvalues and eigenvectors. For this project, the eigenvectors corresponding to the 5 largest eigenvalues were of interest. Then, the eigenvectors are converted to displacements. This is accomplished by taking the unwrapped phase of each eigenvector and subtracting the minimum of each eigenvector from each element in that eigenvector. Then, each element is multiplied by the sampling frequency and divided by the estimated center frequency (via the Loupas Method) and finally multiplied by the displacement per sample to output the PCA estimated displacements (Mauldin, Viola, & Walsker, 2010).

CHAPTER 4: RESULTS

Finite Element Model (FEM) Mesh

Finite element method (FEM) mesh generation resulted in a phantom with quarter symmetry loaded with an ultrasound impulse with a tight focal configuration (F/0.75). This focal configuration served as the push for all simulations. Figure 4-left displays the finely spaced mesh loaded with force corresponding to F/0.75 in LS-DYNA. This spread may be similarly plotted in MATLAB. Figure 4-right displays the same point loads as the figure on the left, additionally indicating the location of the acoustic focal depth. The point loads appear to begin around -13mm rather than extending from the surface of the phantom (0mm). This gap results from thresh-holding which occurs during point load simulation. In reality, some force would be present in the region between -13mm and 0mm and would extend below the hourglass shape.

Figure 4: FEM Mesh with Quarter Symmetry Loaded with F/0.75 Push in LS-DYNA PrePost (left) and in MATLAB (right)

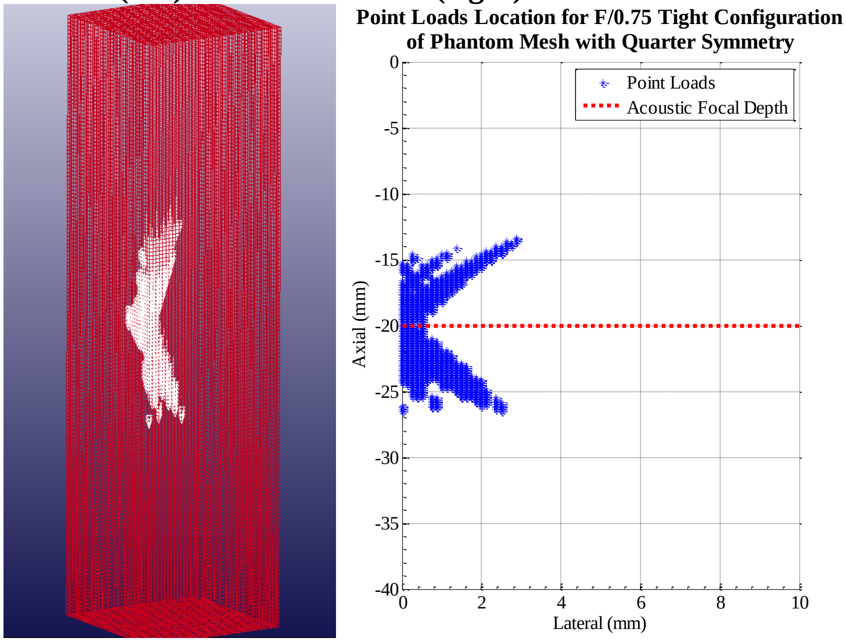

The entire push may be simulated in MATLAB by mirroring the single-quadrant point loads (from Figure 4) over the x and y axes. Figure 5 displays entire F/0.75 points spread forming the hourglass shape characteristic of ultrasound.

Figure 5: FEM Generated Mesh with Entire F/0.75 Point Spread

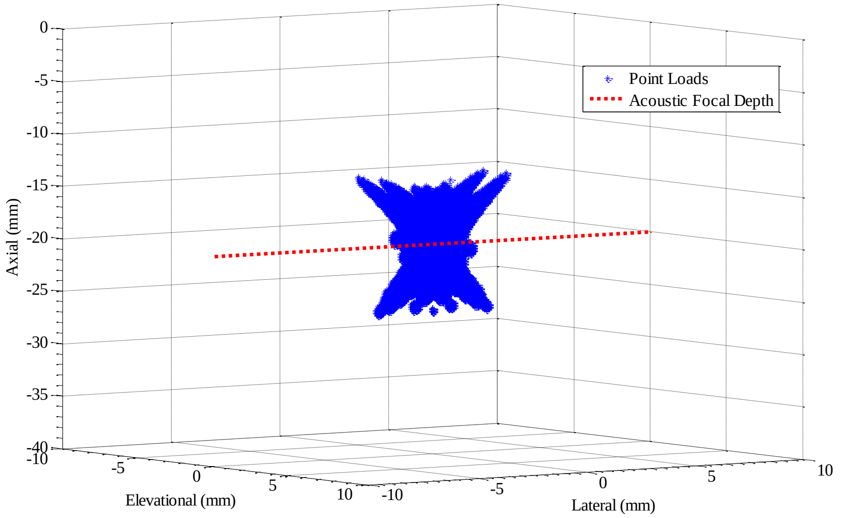

Kernels

Initially, PCA was performed on the entire simulated ultrasound signal matrix. It was hypothesized that the estimated displacement profile for the first eigenvalue (Eig.1) would reflect the initial shear wave, and the second eigenvalue (Eig.2) would show the shear wave later in time, after it had propagated to the edge of the resolution cell. The estimated displacement profiles for 10 scatterer realizations as well as the mean of these signals for Eig.1 are displayed in Figure 6. The signals from Eig.2 are similarly displayed in Figure 7. Subplots increase in Young's Modulus value from left to right across the rows and increase in F/# down the columns. Eig.1 resembles the displacement profile for a shear wave, but Eig.2 does not. At this time, there is no apparent correlation between shear wave propagation and eigenvectors beyond Eig.1. Therefore, only Eig.1 will be discussed herein[2].

---

[2] Additional figures with the 10 seeds and means for Eig.3, Eig.4 and Eig.5 are located in Appendix 1.

Figure 6: 10 Seeds and Mean Displacement Estimation for Eig. 1 of Entire Data Set

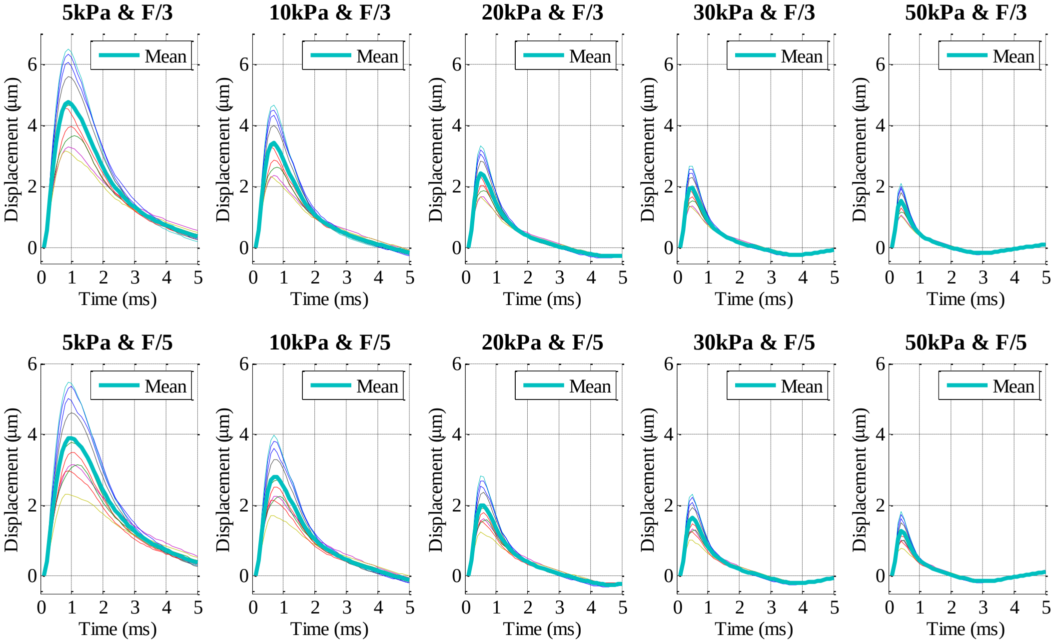

Figure 7: 10 Seeds and Mean Displacement Estimation for Eig. 2 of Entire Data Set

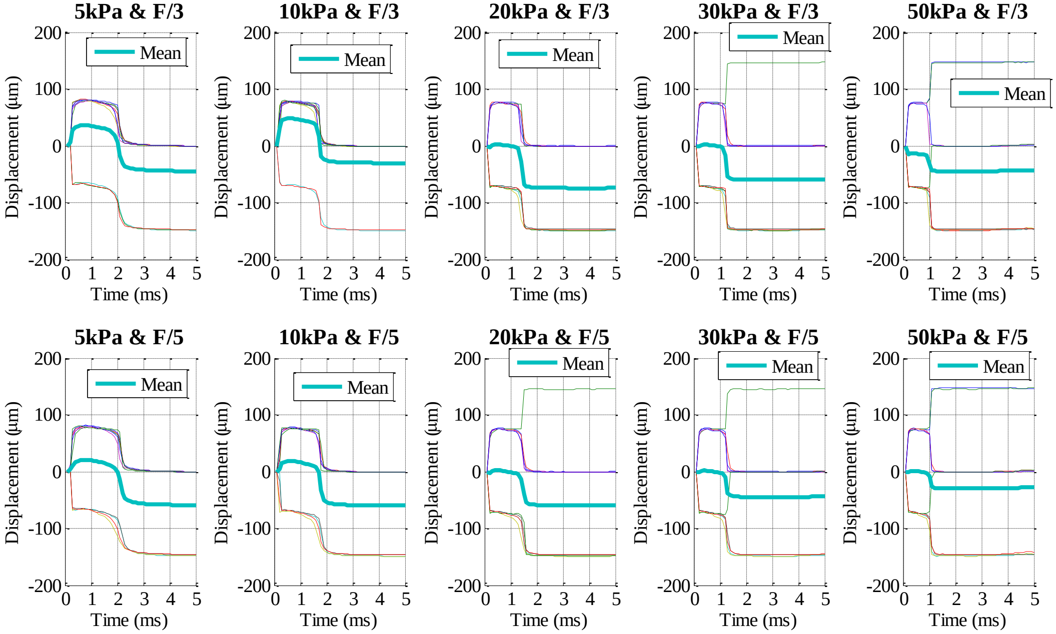

The displacement estimations from these simulations for Eig.1 seemed to be severely underestimating the displacement profiles. Although some underestimation is to be expected with ultrasound, PCA was detecting peak displacements under 6µm for 5kPa and as low as 0.5µm for 50kPa. Small peak displacements can be problematic due to variance between samples. Figure 8 displays the mean estimated displacement profiles of 10 scatterer realizations for Eig.1 from PCA on the entire data set. The error bars indicate standard deviation of the 10 seeds from Figure 6 at each time point. For 5kPa, the mean maximum peak displacement is ~5µm, and the standard deviation is ~1.25µm. In this case, the standard deviation is 25% of the peak displacement.

Figure 8: Mean Displacement Estimation with Standard Deviation for Eig. 1 of Entire Data Set

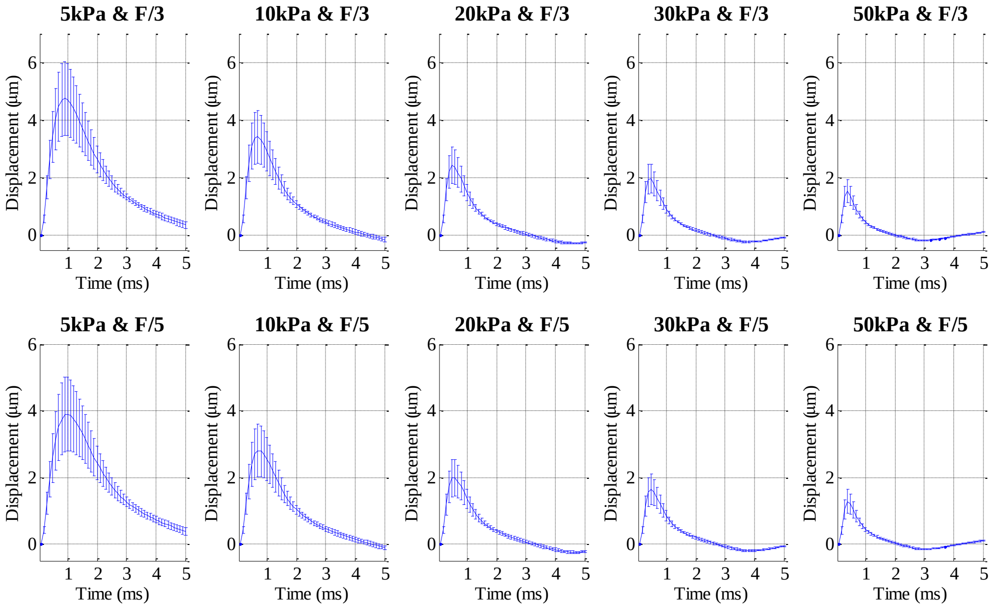

To attempt to reduce this underestimation and make the standard deviations less significant, axial kernels of the data were selected to perform PCA. The process for extracting these subsets was addressed in the methods chapter. Many normalized cross-correlation methods use kernels of 1.5λ, so initially, kernel sizes of 1λ, 1.5λ, and 3λ were selected. Kernel location may also be selected. It was hypothesized that the kernel should be located at the acoustic focal depth (20mm) because this is the depth at which the acoustic radiation force (ARF) is most uniform laterally and in magnitude. Therefore, kernel subsets were initially centered at 20mm. Figure 9 displays the selected axial kernels on the F/0.75 quarter symmetry mesh.

Figure 9: Selected Axial Kernels on F/0.75 Quarter Symmetry Mesh

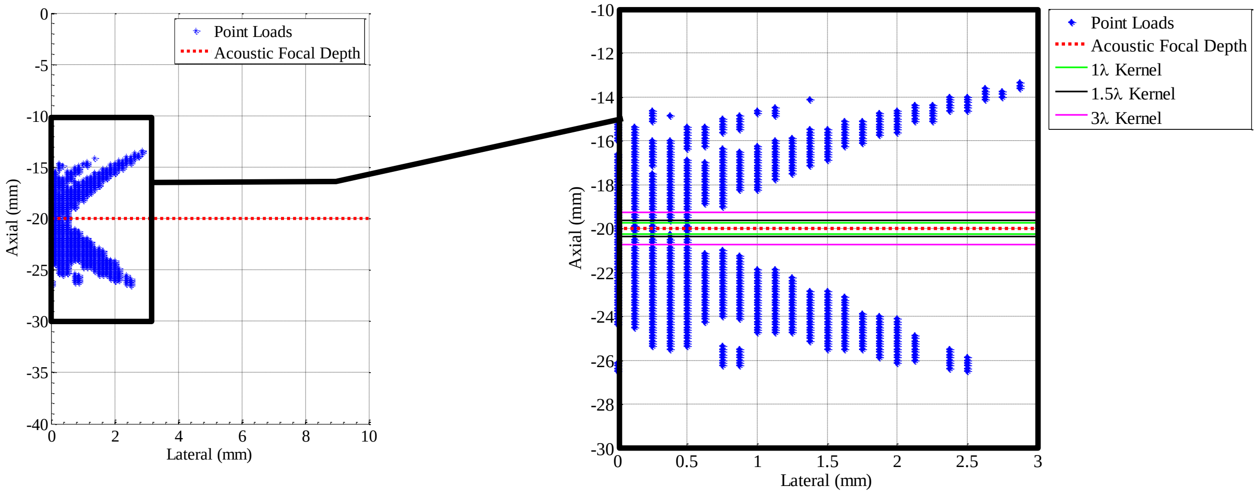

Figure 10 displays the mean estimated displacement profiles for Eig.1 for kernels 1λ, 1.5λ, and 3λ plotted on the same figure as the result of PCA on the entire data set. This figure more clearly shows the underestimation resulting from performing PCA on the entire data set. Therefore, only kernels of data are examined herein.[3]

Figure 10: Mean Displacement Estimation for Eig.1 of Three Kernels focused at 20mm Compared to Eig.1 of the Entire Data Set

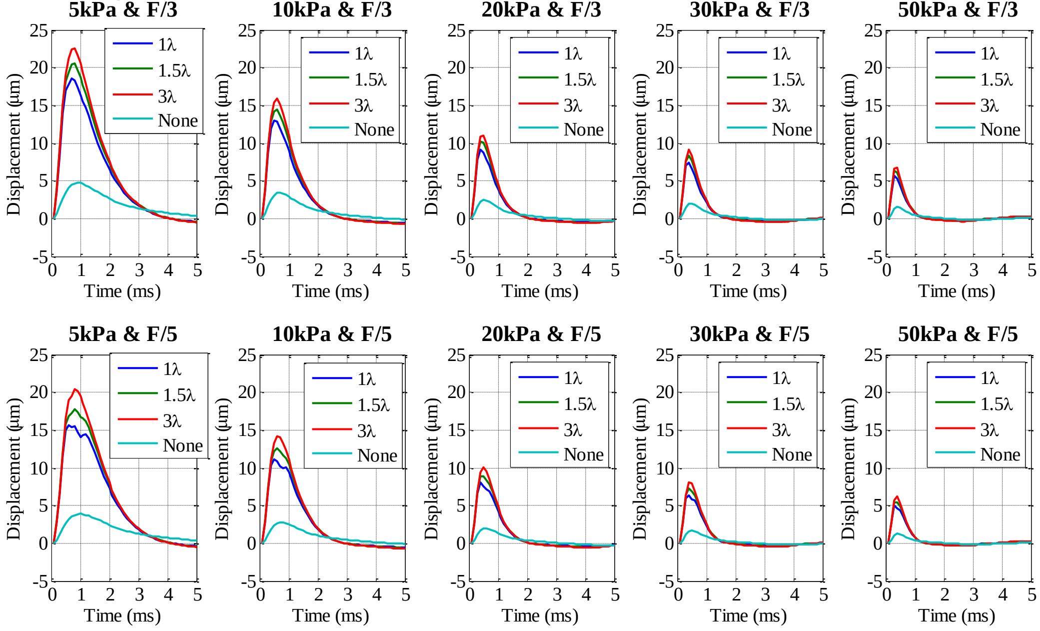

---

[3] Additional figures with for 1λ, 1.5λ, and 3λ Eig.1 are located in Appendix 2

Further examination of the kernels noted that some of the plots were not smooth, but instead featured double peaks. The peaks seemed to be most apparent in the 1λ kernel with F/5 tracking. Therefore, this case will be the focus of the remaining figures and double peak detection and analysis. Although the source of this double peak is unknown, the peaks appear to get closer together in time as stiffness increases. This is also characteristic of shear wave movement—as the material gets stiffer, shear waves may propagate faster. It was hypothesized that shear wave movement was in fact not orthogonal. PCA separates eigenvectors by orthogonality, so if the two cases of shear wave detection were not orthogonal, then they would not be separated into two different eigenvectors. Therefore, it may be possible that the first peak is the initially detected shear wave and the second peak is the shear wave which was detected after it propagated. This suspicion led to an interest in quantifying the change in distance and time between the peaks via shear wave velocity calculations.

In an attempt to determine the source of the double peaks, displacement tracking was performed on the generated displacement data. Simulated tracking is performed by a previously developed script in the lab, ‘createSimResDisp.dat’. This program treats each junction in the mesh like a scatterer, and tracks its displacement over time. The output allows motion tracking through time of a specified location—indicated by x, y, z, coordinates.

In this project, PCA is performed on the simulated ultrasound data, so rather than merely tracking individual nodes, it is more useful to perform averaging. This averaging should be restricted to the resolution cell. The resolution cell size is dependent upon F/#, kernel size, and transducer. The F/# of the tracking beam determines the lateral distance spanned by the resolution cell. The kernel size determines the axial distance spanned by the resolution cell. Since the transducer used for this application is 1D linear array, the elevational distance of the resolution cell is fixed. Figure 11 depicts the results of displacement tracking with averaging, focused at 20mm. Figure 11 additionally includes the displacement estimation for 1λ to allow comparison between the two waveforms. The estimated profile underestimates the result from the displacement tracking.

Figure 11: Mean Displacement Estimation (Eig.1) Comparison to Mean Displacement Tracking for 1λ Focused at 20mm

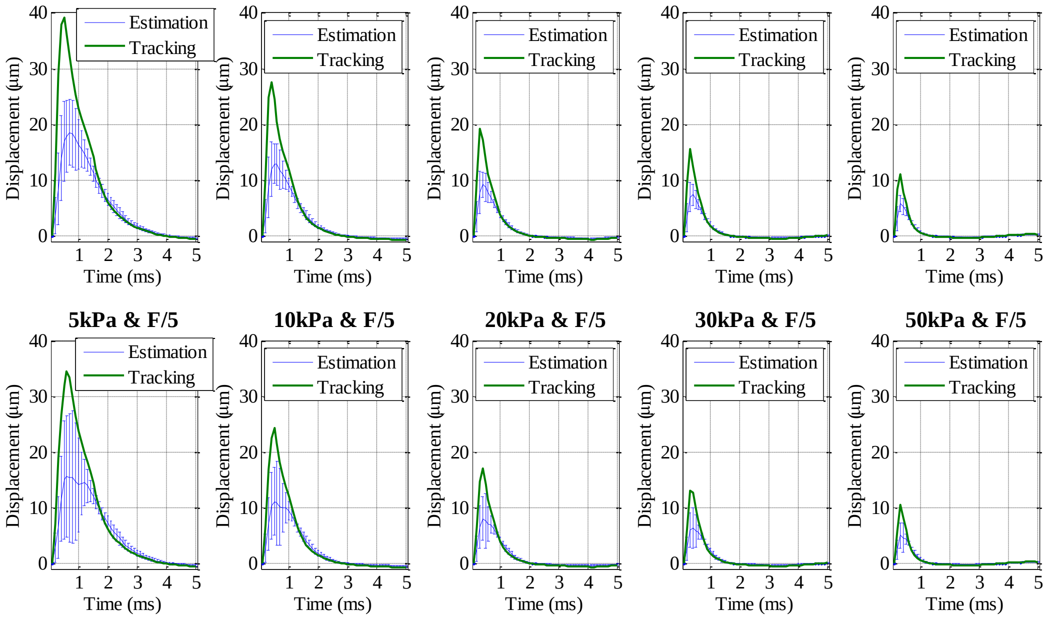

Velocity Computation

This application attempts to develop a method of measuring shear wave velocity as a way to determine tissue stiffness. Once the experimental velocity is determined, it may be compared to the expected shear wave velocity. Since the phantoms were designed with specific Young's modulus values (E), density (ρ), and Poisson Ratio (v), the expected shear wave velocity (c_t) may be calculated. For these simulations, density was 1 g/m^3, and Poisson's Ratio was 0.499. With these constants, shear wave velocity may be defined only in relation to Young's Modulus:

$$c_t = \sqrt{\frac{E}{2(1+v)\rho}} \cong \sqrt{\frac{E}{3}}.$$

Table 1 includes the expected shear wave velocities for the Young's modulus values simulated.

Table 1: Expected Shear Wave Velocities for Simulated Young's Modulus Values

Young's Modulus (E)	Expected Velocity (c_t)
5kPa	1.29 m/s
10kPa	1.83 m/s
20kPa	2.58 m/s
30kPa	3.16 m/s
50kPa	4.08 m/s

Experimental shear wave velocity may be calculated using the change in time between the double peaks. To determine the time span between the peaks, the "findpeaks" MATLAB function was used to locate maxima of the signal. This script was not tailored to this application, so it was not able to detect all peaks. For 20kPa, 30kPa, and 50kPa, the second peak was not detected using this function, so the location was selected manually. Once the double peaks were located, the change in time between the peaks was calculated and displayed on the plot.

Previously, it was noted that the kernels were centered at 20mm because this is the acoustic focal depth. In reality, kernels with the center shifted slightly up or down axially will still satisfy the condition of containing uniform force within the kernel. For this reason, the kernel was shifted axially to find the optimal location for displaying the double peaks. Although visually many locations displayed the double peaks, the "findpeaks" function extracted the peaks for some locations more successfully than others. Therefore, Figure 12 displays the 1λ kernel for F/5 tracking at 20.03 mm. This figure indicates the detected double peaks and change in time (Δt) on each plot. The change in time values are also located in Table 2. Although the change in time for 30kPa and 50kPa are equal, this is likely due to the fact that the simulation extracted displacements in 0.1ms increments. This limits the change in time resolution for all Young's Modulus values, but it becomes more apparent in the stiffer materials, in which the shear wave propagates fastest.

Figure 12: Double Peak Detection for 1λ, Eig.1, at 20.03mm

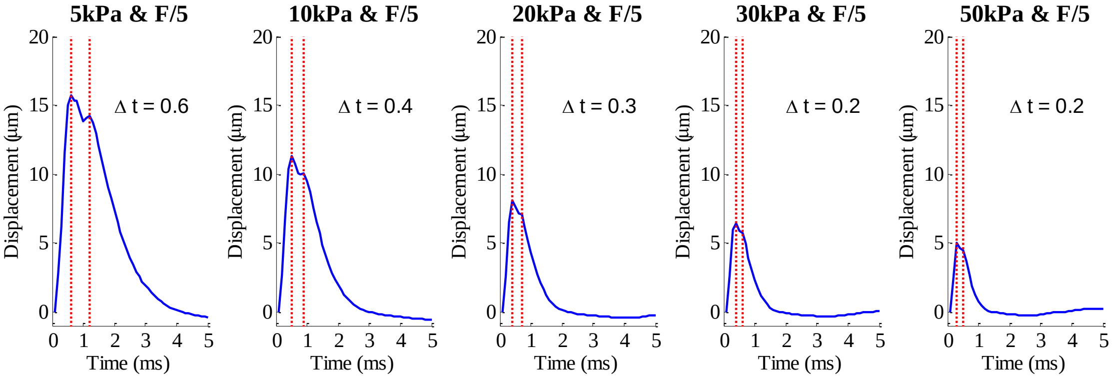

Experimental shear wave velocity ($c_{t,exp}$) may be calculated by taking the change in distance (Δ*d*) over the change in time (Δ*t*):

$$c_{t,exp} = \frac{\Delta d}{\Delta t}.$$

Initially, it was predicted that the change in distance would equal half the lateral span of the resolution cell. Therefore, the predicted change in distance may be calculated using F/# and wavelength (λ):

$$\Delta d = \frac{1}{2} F/\# * \lambda .$$

For the F/5 tracking case, the change in distance (Δ*d*) would therefore be 626µm. The experimental velocity—calculated using this change in distance—is displayed in Table 2.

Table 2: Experimental Shear Wave Velocities for Simulated Young's Modulus Values Using Time Between Double Peaks as Change in Time for F/5

Young's Modulus (E)	Change in Time Between Peaks (Δt)	Experimental Velocity ($c_{t,exp}$)	Percent Error (%)
5kPa	0.6 ms	1.04 m/s	19
10kPa	0.4 ms	1.57 m/s	14
20kPa	0.3 ms	2.09 m/s	19
30kPa	0.2 ms	3.13 m/s	1
50kPa	0.2 ms	3.13 m/s	23

The experimental shear wave velocities were an order of magnitude off from the expected shear wave velocities. This is likely due to the selection of change in distance as half the lateral span of the resolution cell. In reality, it is unclear at what point PCA extracted the second peak, so this distance estimation may be incorrect. To see if the experimental shear wave velocity is even related to Young's Modulus, the ratios of the experimental velocities by Young's Modulus values were compared to the expected velocities ratios. It was hypothesized that the 30kPa or 50kPa ratios would have the largest error due to the time resolution issue previously addressed. Superficially, this appears to be true from the data in Table 2 because the experimental velocities for 30kPa and 50kPa are identical when the velocity for 50kPa is expected to be faster than 30kPa. Table 3 includes these values and the percent error of the experimental ratio compared to the expected ratio. The ratios including 30kPa (rows indicated in grey) had the largest percent error, ranging from 14% to 30%. This percent error is significantly higher than those of the other Young's Modulus values. The mean of the absolute values of the percent errors was 11%.

Table 3: Expected and Experimental Shear Wave Velocities Ratios and Percent Error for Double Peaks

Young's Modulus Ratio	Expected Ratio	Experimental Ratio	Percent Error (%)
5kPa/10kPa	0.71	0.67	-6
5kPa/20kPa	0.50	0.50	0
5kPa/30kPa	0.41	0.33	-20
5kPa/50kPa	0.32	0.33	3
10kPa/20kPa	0.71	0.75	6
10kPa/30kPa	0.58	0.50	-14
10kPa/50kPa	0.45	0.50	11
20kPa/30kPa	0.82	0.67	-18
20kPa/50kPa	0.63	0.67	6
30kPa/50kPa	0.77	1	30

Shear wave velocity may also be calculated relatively. This may be accomplished by comparing the time-to-peak (TTP) or time-to-recovery (TTR) for the F/3 and F/5 shear waves. Figure 13 shows the TTP for 1λ kernel at 20.03 mm and indicates the value of the TTP for each plot. It was hypothesized that the difference between the TTP for F/3 and F/5 could be used to calculate the experimental velocity. From Figure 13, it is clear that this was not possible because the 5kPa difference was the only TTP difference not equal to zero. This process was repeated for 1.5λ and 3λ kernels, but the same problem resulted. Those figures are located in Appendix 2.

Figure 13: Time-to-Peak (TTP) Detection for 1λ, Eig.1, at 20.03mm

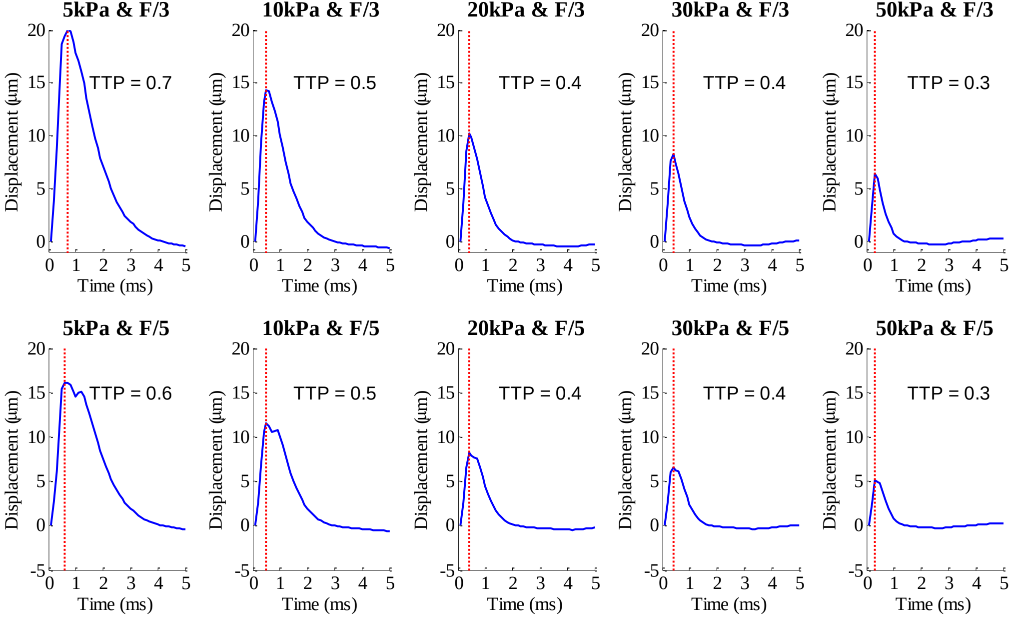

Time-to-recovery (TTR) is the timespan over which at which the waveform has recovered 2/3 of the way from its peak. Figure 14 shows the TTR for 1λ kernel at 20.03 mm and indicates the value of the TTP for each plot. It was hypothesized that the difference between the TTP for F/3 and F/5 could be used to calculate the experimental velocity. The change in distance (Δd) for this method is the difference between half the lateral span of the resolution cells for F/3 and F/5. This distance can be calculated in terms of wavelength (λ) and F/# similar:

$$\Delta d = \frac{1}{2}(F/5 - F/3) * \lambda.$$

Therefore, the change in distance (Δ*d*) is 250 µm. Table 4 shows the TTR from each plot, the difference in time to peak between F/3 and F/5 for each Young's Modulus value, and the experimental velocity. The mean of the absolute values of the percent errors was 11%.

Figure 14: Time-to-Recovery (TTR) Detection for 1λ, Eig.1, at 20.03mm

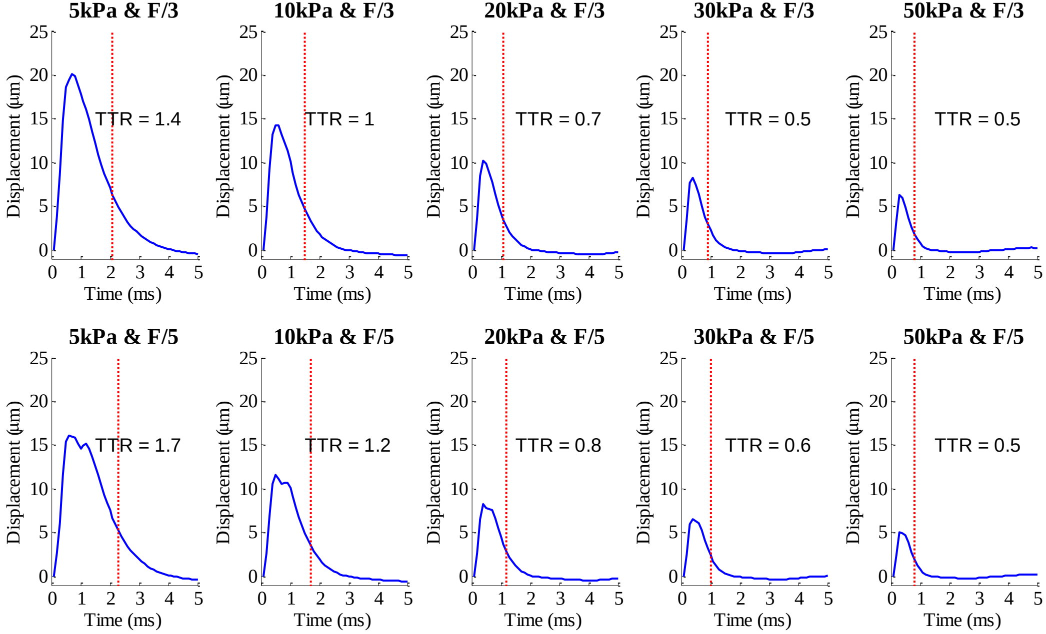

Table 4: Experimental Shear Wave Velocities for Simulated Young's Modulus Values Using Time-to-Recovery (TTR) as Change in Time

Young's Modulus (E)	F/#	TTR	Difference in TTR (Δt)	Experimental Velocity ($c_{t,exp}$)	Percent Error (%)
5kPa	F/3	1.4 ms	0.3 ms	0.83 m/s	36
	F/5	1.7 ms			
10kPa	F/3	1 ms	0.2 ms	1.25 m/s	31
	F/5	1.2 ms			
20kPa	F/3	0.7 ms	0.1 ms	2.50m/s	3
	F/5	0.8 ms			
30kPa	F/3	0.5 ms	0.1 ms	2.50 m/s	20
	F/5	0.6 ms			
50kPa	F/3	0.5 ms	0 ms	n/a	n/a
	F/5	0.5 ms			

Similar to the double peak results for experimental shear wave velocity, these experimental shear wave velocities were an order of magnitude off from the expected shear wave velocities. This is also likely due to the selection of change in distance as half the lateral span of the resolution cell. The same ratio method was conducted for these experimental shear wave velocities. Table 4 includes these values and the percent error of the experimental ratio compared to the expected ratio. The ratios including 50kPa (rows indicated in grey) could not be calculated due to the lack of experimental velocity. The other ratios (rows indicated in grey) ranged from 6% to 34% error. The mean of the absolute values of the percent errors was 21%.

Table 5: Expected and Experimental Shear Wave Velocities Ratios and Percent Error for Time to Recovery (TTR)

Young's Modulus Ratio	Expected Ratio	Experimental Ratio	Percent Error (%)
5kPa/10kPa	0.71	0.67	-6
5kPa/20kPa	0.50	0.33	-34
5kPa/30kPa	0.41	0.33	-20
5kPa/50kPa	0.32	n/a	n/a
10kPa/20kPa	0.71	0.50	-30
10kPa/30kPa	0.58	0.50	-14
10kPa/50kPa	0.45	n/a	n/a
20kPa/30kPa	0.82	1	22
20kPa/50kPa	0.63	n/a	n/a
30kPa/50kPa	0.77	n/a	n/a

CHAPTER 5: CONCLUSION & FUTURE DIRECTION

This project attempted to use PCA to reconstruct shear waves propagating away from the region of excitation (ROE) of an acoustic radiation force impulse. It was hypothesized that by using a narrowly focused push beam (F/0.75) and a wide track beam (F/3 or F/5), it would be possible to detect the shear wave propagation. Furthermore, it was hypothesized that the first eigenvalue extracted by PCA would encode information on the initial shear wave, and the second eigenvalue would encode information on the shear wave later in time, once it had propagated away from the ROE. At this time eigenvalues beyond the first do not seem to encode any information regarding shear wave propagation.

Although the initial hypothesis did not hold, double peaks—not characteristic of shear wave waveforms—were detected in certain kernels of the F/5 tracked eigenvector 1. Future work will need to be conducted to investigate why certain kernels displayed this double peak more prominently than others. The detection of double peaks led to a new hypothesis that PCA had merged what was expected to be two separate signals into the same eigenvector. This would make sense if the waveforms were not orthogonal. As stiffness increased, the distance between the two peaks appeared to decrease. This would make sense if these peaks indicated two different times at which the shear wave was detected because shear waves propagate faster in stiffer materials.

At this time, it is still unclear where the second shear wave (i.e. the second peak) was detected. Initially, it was hypothesized that it was extracted from the edge of the resolution cell. This would mean that the time between the peaks would indicate the time it took the shear wave to span half of the resolution cell. Calculation of experimental shear wave velocity based on this hypothesis resulted in velocities an order of magnitude lower than the expected shear wave velocity. The results were limited by the time resolution of the samples, 0.1ms. Although the experimental shear wave velocities were not accurate, the ratios of the shear wave velocities for different stiffnesses resulted in values within 11% of the expected shear wave velocities. If the distance corresponding to the timespan between the peaks can be determined, this method may be valid way of measuring shear velocity quantitatively.

Other methods of relatively measuring shear wave velocity were also attempted: time-to-peak and time-to-recovery. Time-to-peak was not successful because the difference in time-to-peak for F/3 and F/5 for most stiffness was equal to zero. The difference in time-to-recovery for F/3 and F/5 were different, but the experimental shear wave velocities calculated in this method were also an order of magnitude too small. When the ratios for time-to-recovery velocities were compared to the expected velocities, there was significantly more error than the results from the double peaks method. Before dismissing either time-to-peak or time-to-recovery, it would be useful to examine other kernels as well as other focuses of the kernels (beyond 20mm).

Although more work needs to do be done in simulation, the hope is that this work will be implemented in tissue mimicking phantoms. These phantoms may be constructed from materials with the same Young’s modulus values used in simulation. This will allow the experimental results to be compared to the simulated ones. Following testing in tissue mimicking materials, this method will eventually be implemented in tissue.

APPENDIX 1: SUPPLEMENTARY MATLAB FIGURES FOR ENTIRE DATA SET

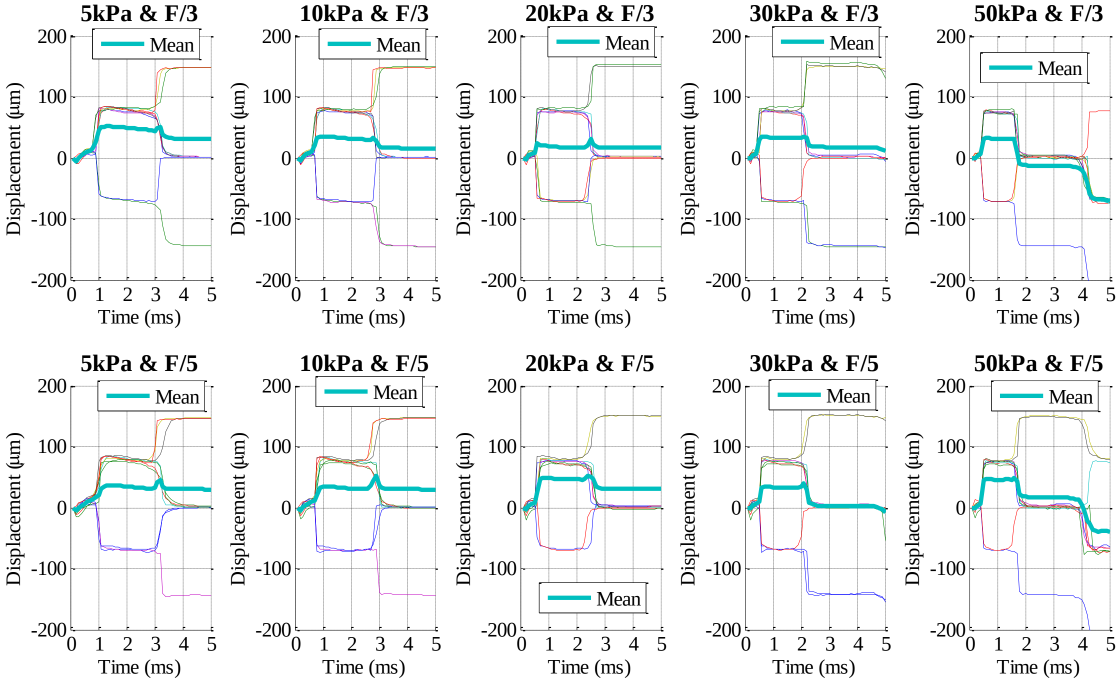

10 Seeds and Mean for No Kernel, Eig.3

5kPa & F/3, 10kPa & F/3, 20kPa & F/3, 30kPa & F/3, 50kPa & F/3

5kPa & F/5, 10kPa & F/5, 20kPa & F/5, 30kPa & F/5, 50kPa & F/5

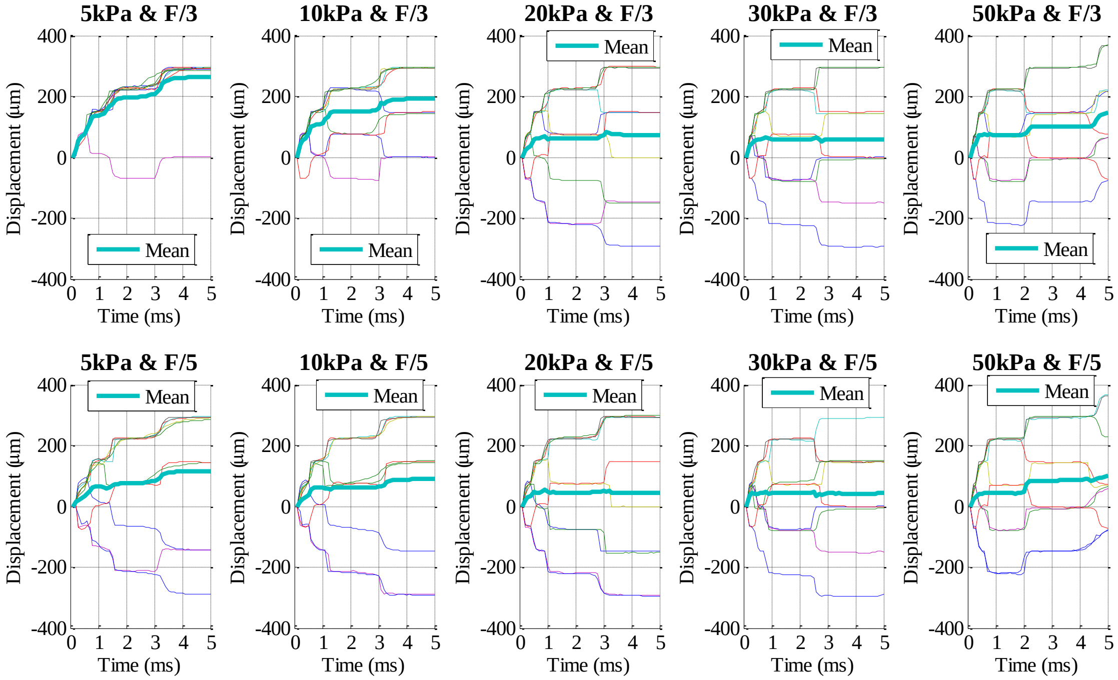

10 Seeds and Mean for No Kernel, Eig.4

5kPa & F/3, 10kPa & F/3, 20kPa & F/3, 30kPa & F/3, 50kPa & F/3

5kPa & F/5, 10kPa & F/5, 20kPa & F/5, 30kPa & F/5, 50kPa & F/5

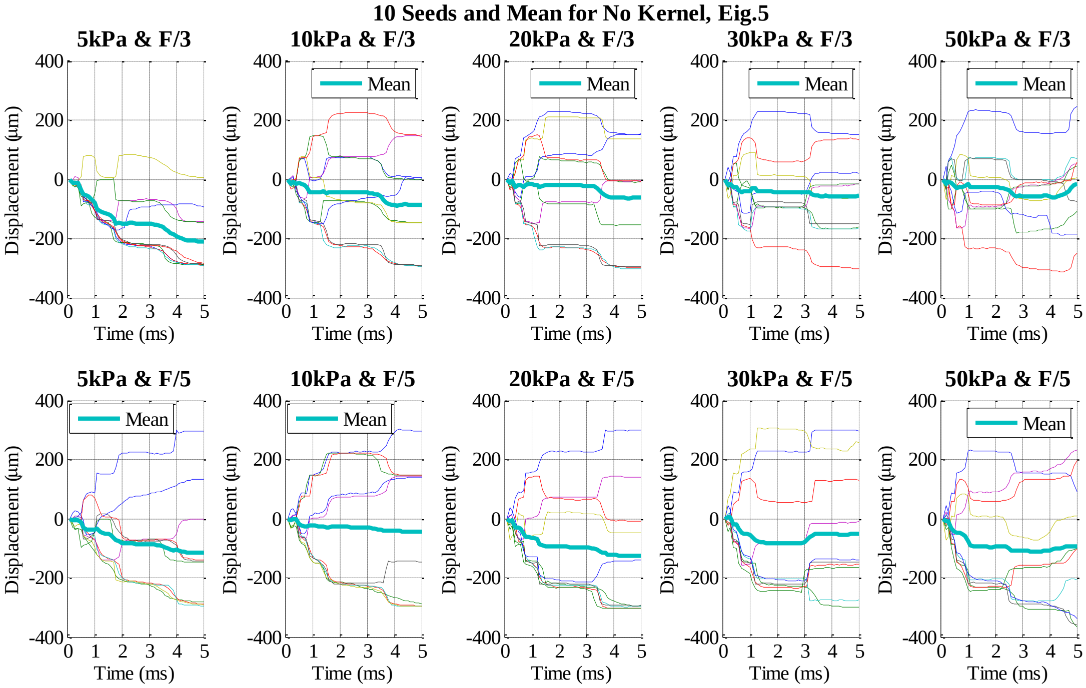
10 Seeds and Mean for No Kernel, Eig.5
5kPa & F/3
10kPa & F/3
20kPa & F/3
30kPa & F/3
50kPa & F/3
5kPa & F/5
10kPa & F/5
20kPa & F/5
30kPa & F/5
50kPa & F/5
Mean
Displacement (μm)
Time (ms)
400
200
0
-200
-400
0 1 2 3 4 5

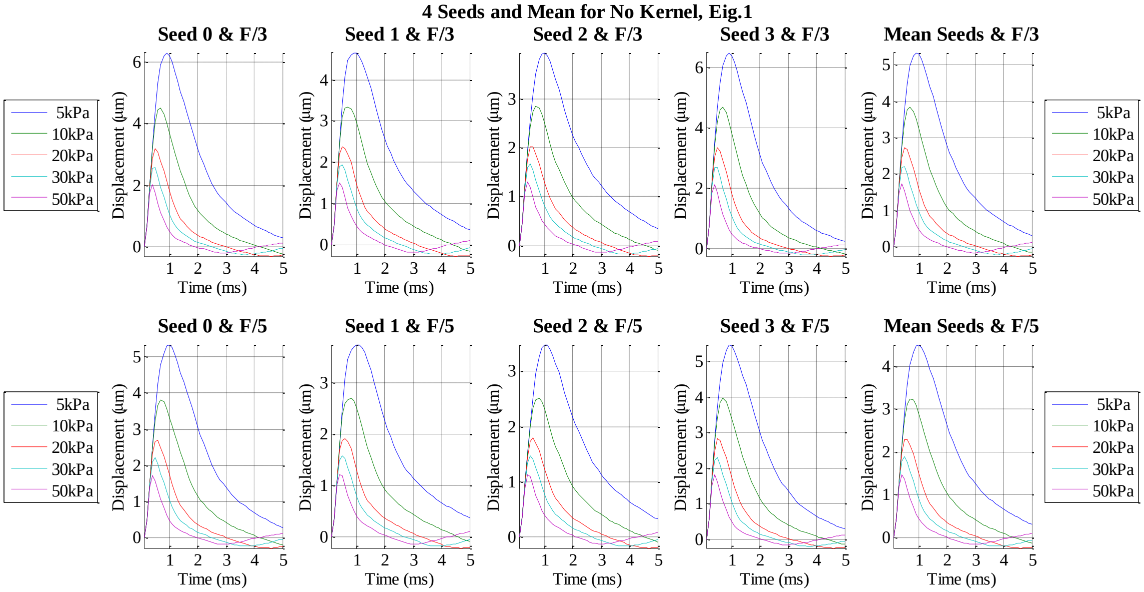
4 Seeds and Mean for No Kernel, Eig.1
Seed 0 & F/3
Seed 1 & F/3
Seed 2 & F/3
Seed 3 & F/3
Mean Seeds & F/3
Seed 0 & F/5
Seed 1 & F/5
Seed 2 & F/5
Seed 3 & F/5
Mean Seeds & F/5
5kPa
10kPa
20kPa
30kPa
50kPa
Displacement (μm)
Time (ms)
1 2 3 4 5

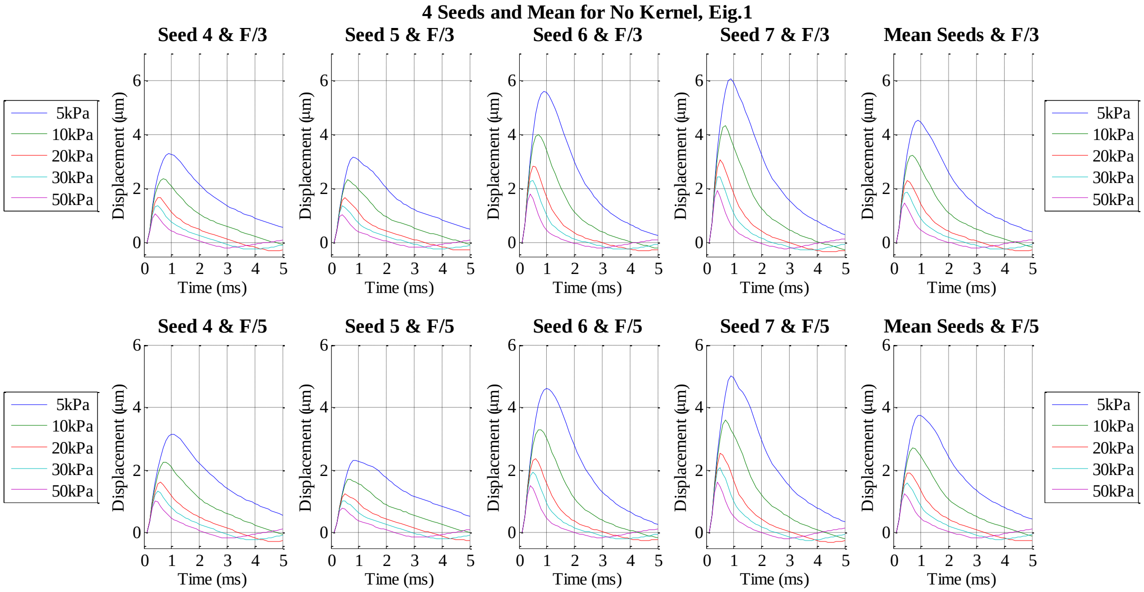

4 Seeds and Mean for No Kernel, Eig.1

Seed 4 & F/3

Seed 5 & F/3

Seed 6 & F/3

Seed 7 & F/3

Mean Seeds & F/3

Seed 4 & F/5

Seed 5 & F/5

Seed 6 & F/5

Seed 7 & F/5

Mean Seeds & F/5

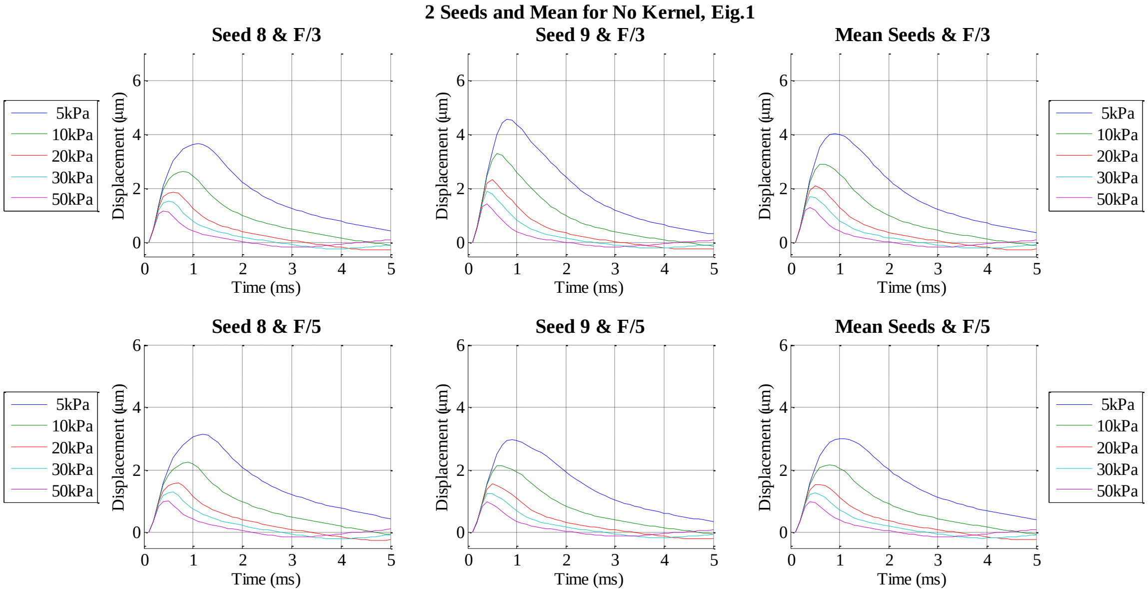

2 Seeds and Mean for No Kernel, Eig.1

Seed 8 & F/3

Seed 9 & F/3

Mean Seeds & F/3

Seed 8 & F/5

Seed 9 & F/5

Mean Seeds & F/5

APPENDIX 2: SUPPLEMENTARY MATLAB FIGURES FOR KERNELS

1λ Figures

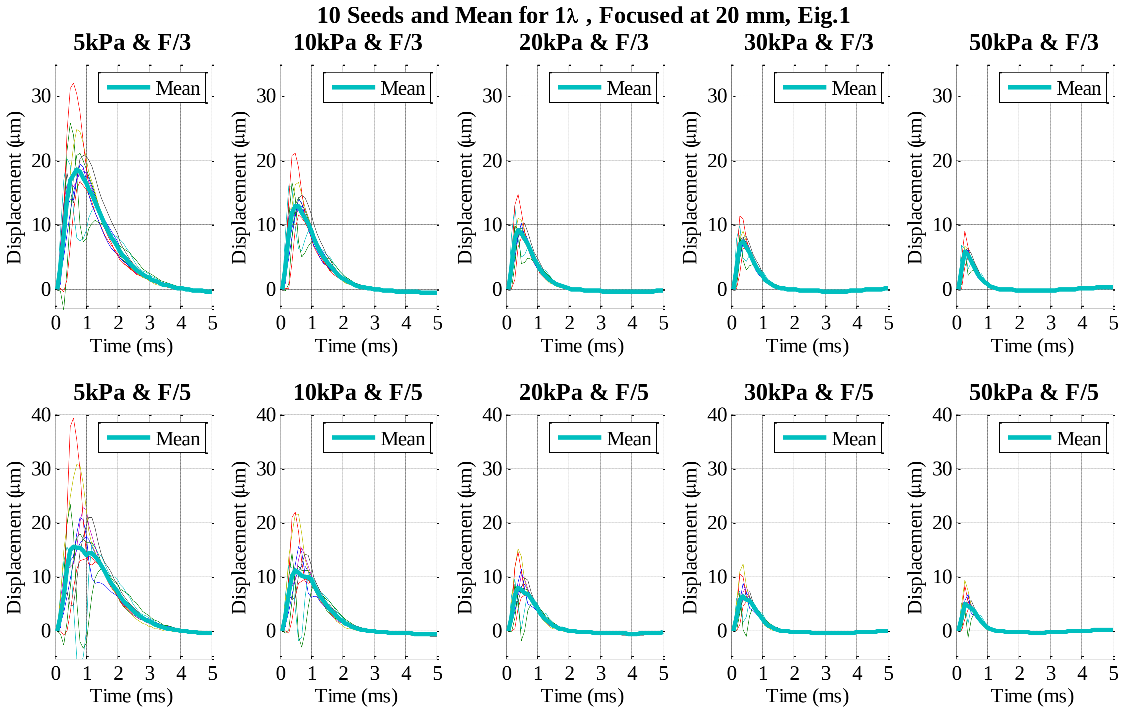

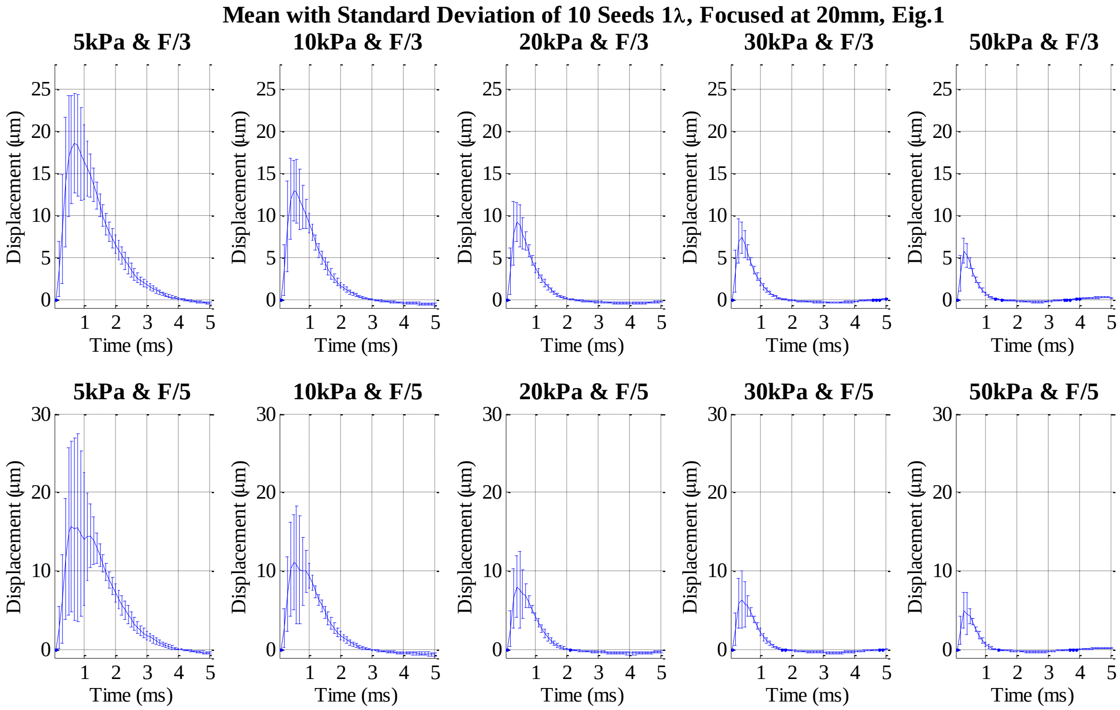

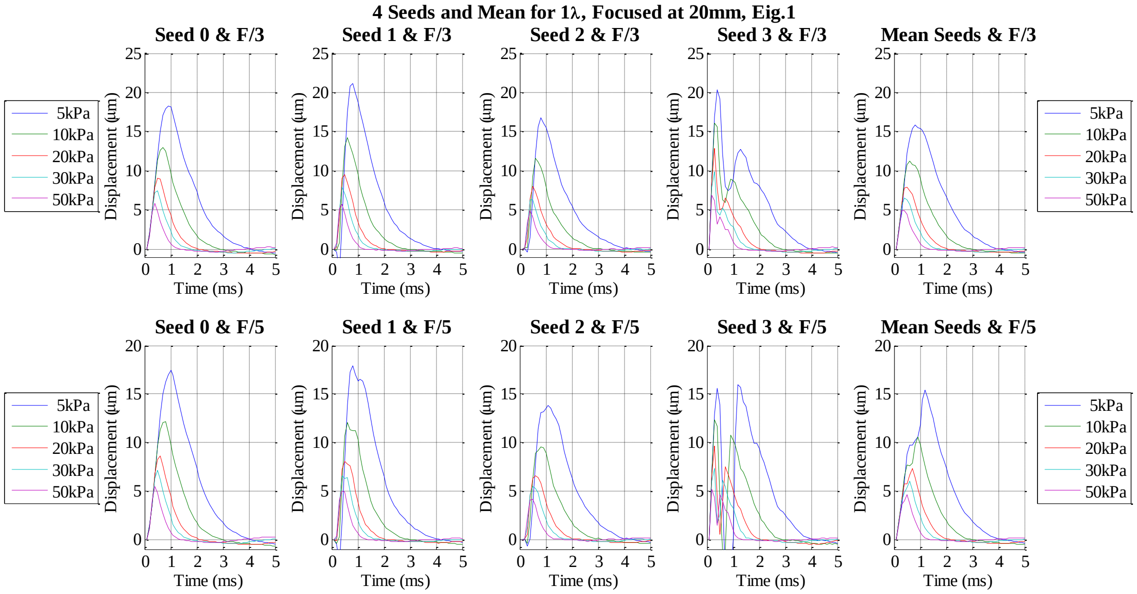
4 Seeds and Mean for 1λ, Focused at 20mm, Eig.1
Seed 0 & F/3
Seed 1 & F/3
Seed 2 & F/3
Seed 3 & F/3
Mean Seeds & F/3
Seed 0 & F/5
Seed 1 & F/5
Seed 2 & F/5
Seed 3 & F/5
Mean Seeds & F/5
Displacement (μm)
Time (ms)
0
5
10
15
20
25
0 1 2 3 4 5
5kPa
10kPa
20kPa
30kPa
50kPa

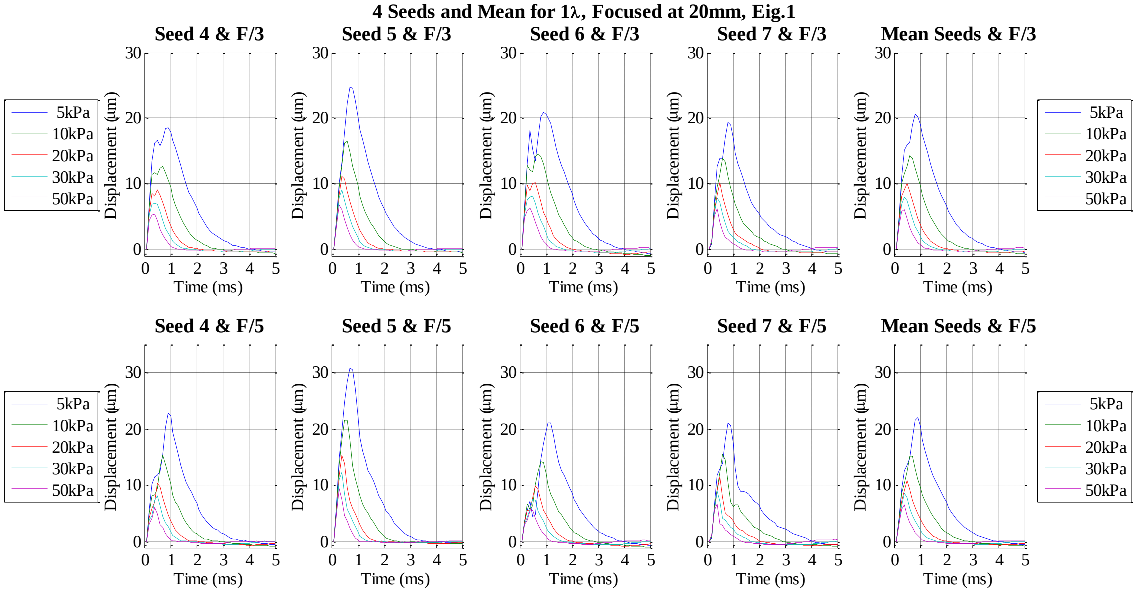
4 Seeds and Mean for 1λ, Focused at 20mm, Eig.1
Seed 4 & F/3
Seed 5 & F/3
Seed 6 & F/3
Seed 7 & F/3
Mean Seeds & F/3
Seed 4 & F/5
Seed 5 & F/5
Seed 6 & F/5
Seed 7 & F/5
Mean Seeds & F/5
Displacement (μm)
Time (ms)
0
10
20
30
0 1 2 3 4 5
5kPa
10kPa
20kPa
30kPa
50kPa

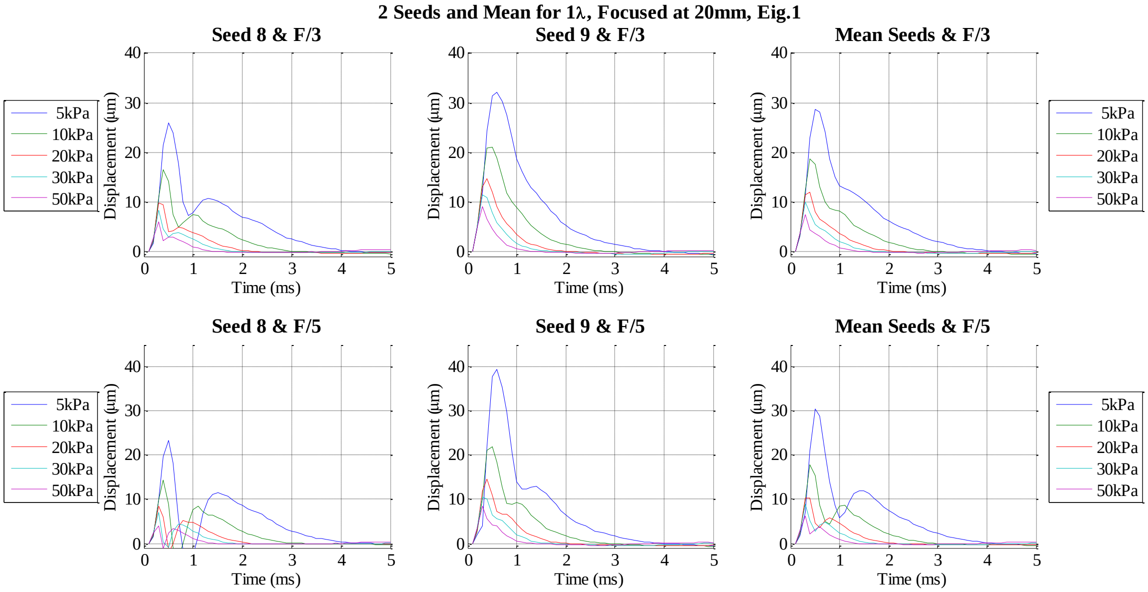
2 Seeds and Mean for 1λ, Focused at 20mm, Eig.1

1.5λ Figures

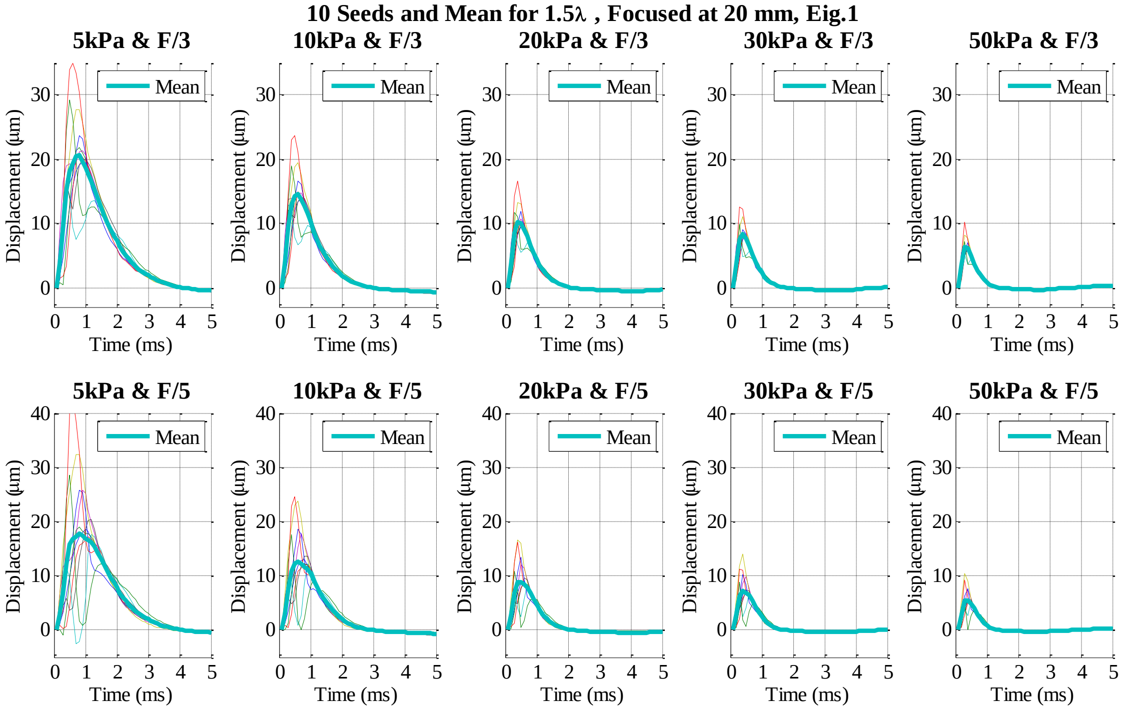
10 Seeds and Mean for 1.5λ , Focused at 20 mm, Eig.1

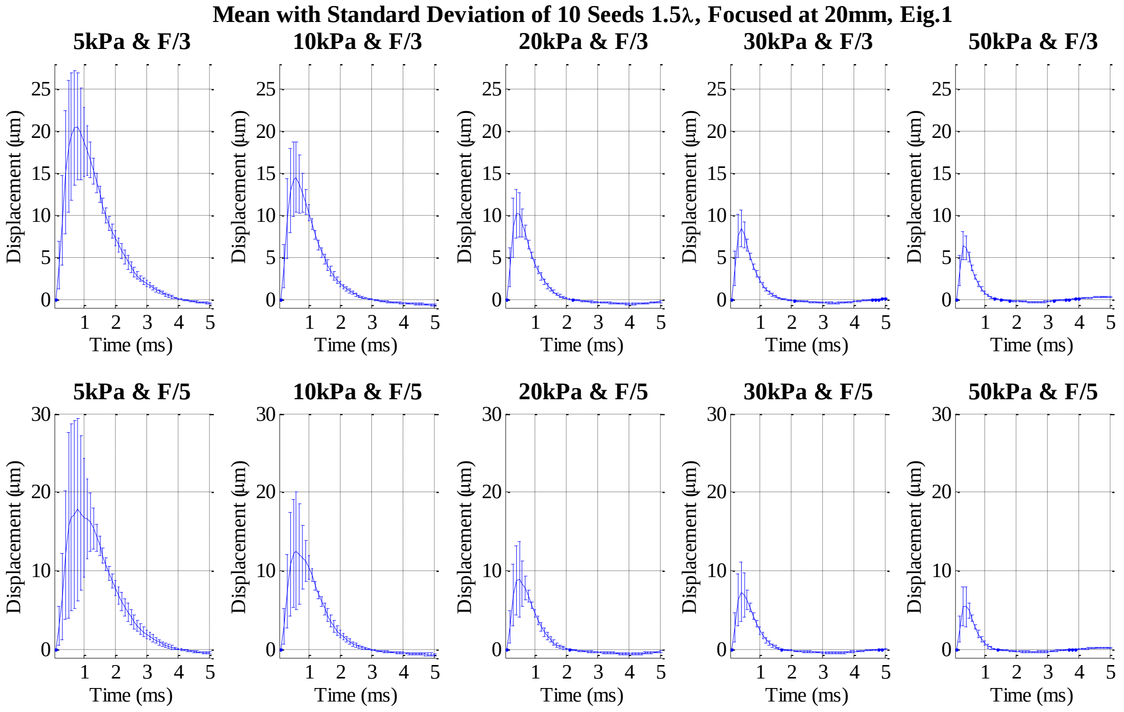
Mean with Standard Deviation of 10 Seeds 1.5λ, Focused at 20mm, Eig.1
5kPa & F/3
10kPa & F/3
20kPa & F/3
30kPa & F/3
50kPa & F/3
5kPa & F/5
10kPa & F/5
20kPa & F/5
30kPa & F/5
50kPa & F/5
Displacement (μm)
Time (ms)
0
5
10
15
20
25
30
1
2
3
4
5

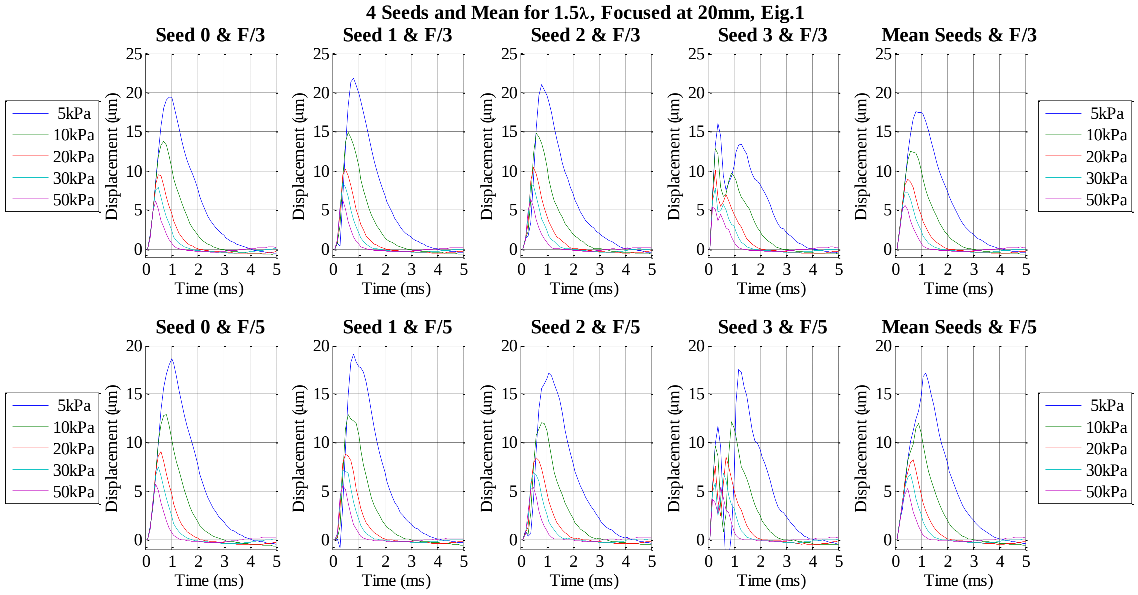
4 Seeds and Mean for 1.5λ, Focused at 20mm, Eig.1
Seed 0 & F/3
Seed 1 & F/3
Seed 2 & F/3
Seed 3 & F/3
Mean Seeds & F/3
Seed 0 & F/5
Seed 1 & F/5
Seed 2 & F/5
Seed 3 & F/5
Mean Seeds & F/5
5kPa
10kPa
20kPa
30kPa
50kPa
Displacement (μm)
Time (ms)
0
5
10
15
20
25
1
2
3
4
5

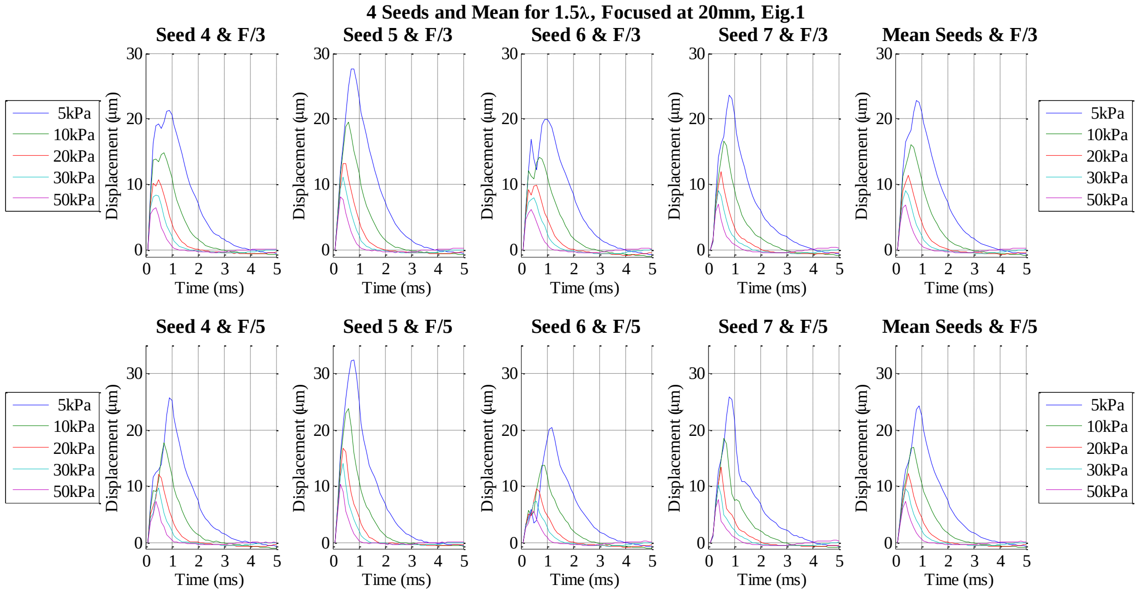
4 Seeds and Mean for 1.5λ, Focused at 20mm, Eig.1
Seed 4 & F/3
Seed 5 & F/3
Seed 6 & F/3
Seed 7 & F/3
Mean Seeds & F/3
Seed 4 & F/5
Seed 5 & F/5
Seed 6 & F/5
Seed 7 & F/5
Mean Seeds & F/5
Displacement (μm)
Time (ms)
0
10
20
30
0
1
2
3
4
5
5kPa
10kPa
20kPa
30kPa
50kPa

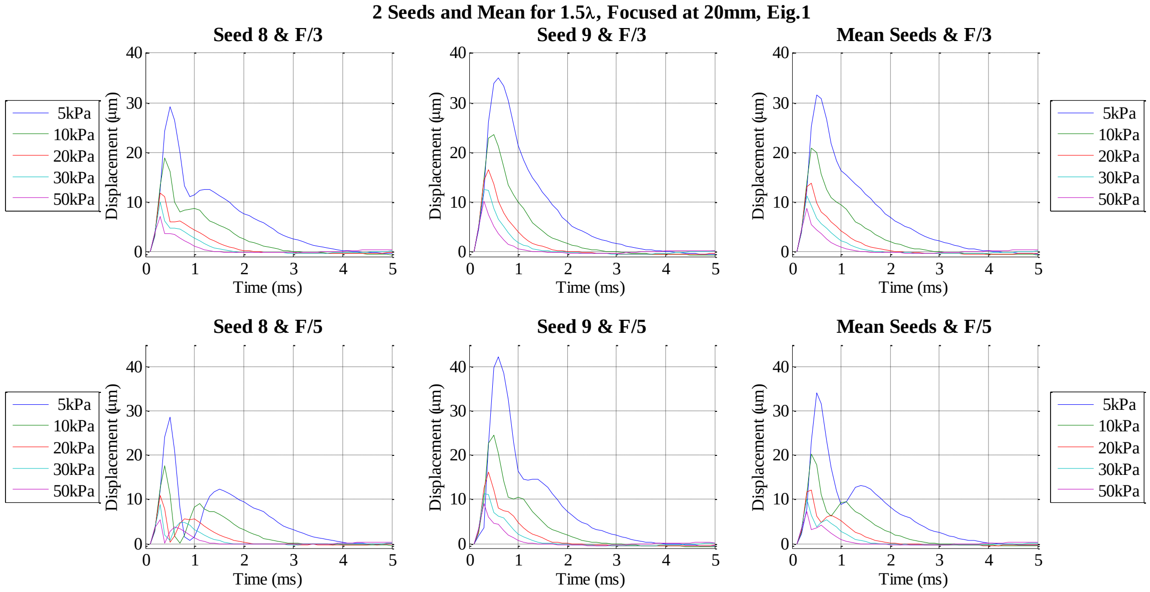
2 Seeds and Mean for 1.5λ, Focused at 20mm, Eig.1
Seed 8 & F/3
Seed 9 & F/3
Mean Seeds & F/3
Seed 8 & F/5
Seed 9 & F/5
Mean Seeds & F/5
Displacement (μm)
Time (ms)
0
10
20
30
40
0
1
2
3
4
5
5kPa
10kPa
20kPa
30kPa
50kPa

3λ Figures

10 Seeds and Mean for 3λ , Focused at 20 mm, Eig.1

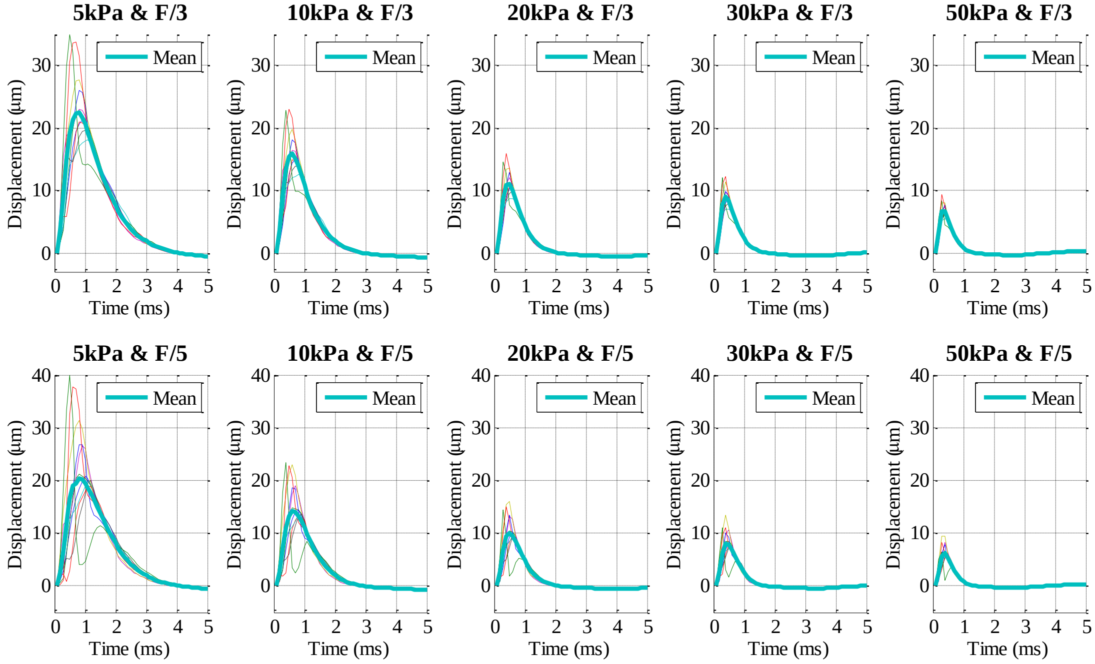

Mean with Standard Deviation of 10 Seeds 3λ, Focused at 20mm, Eig.1

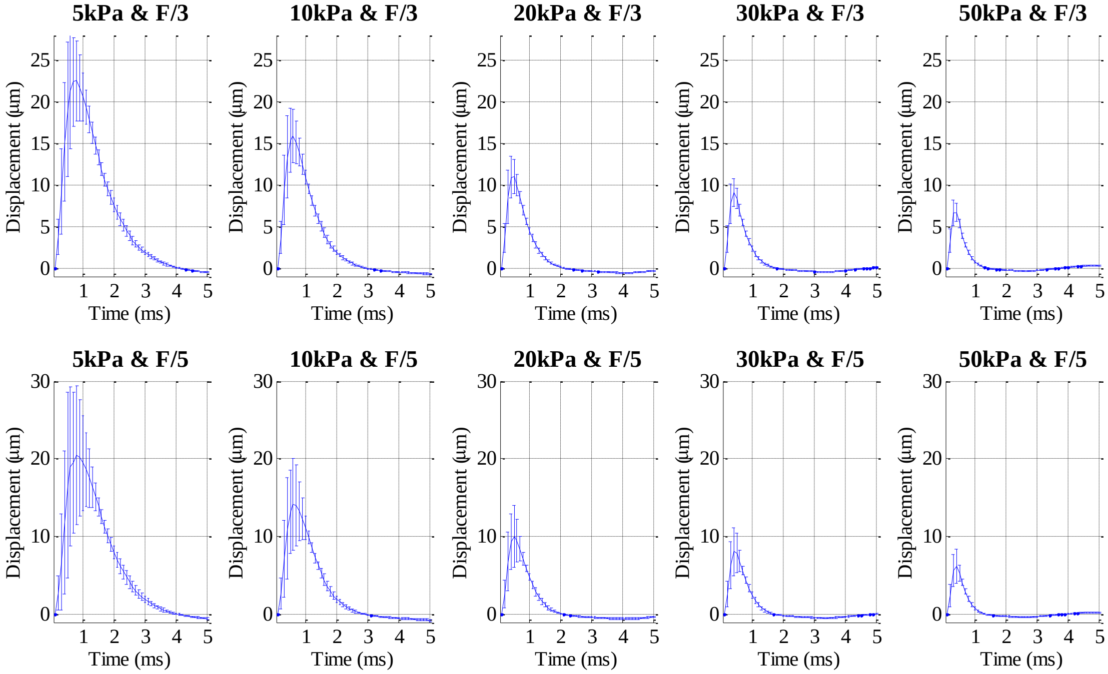

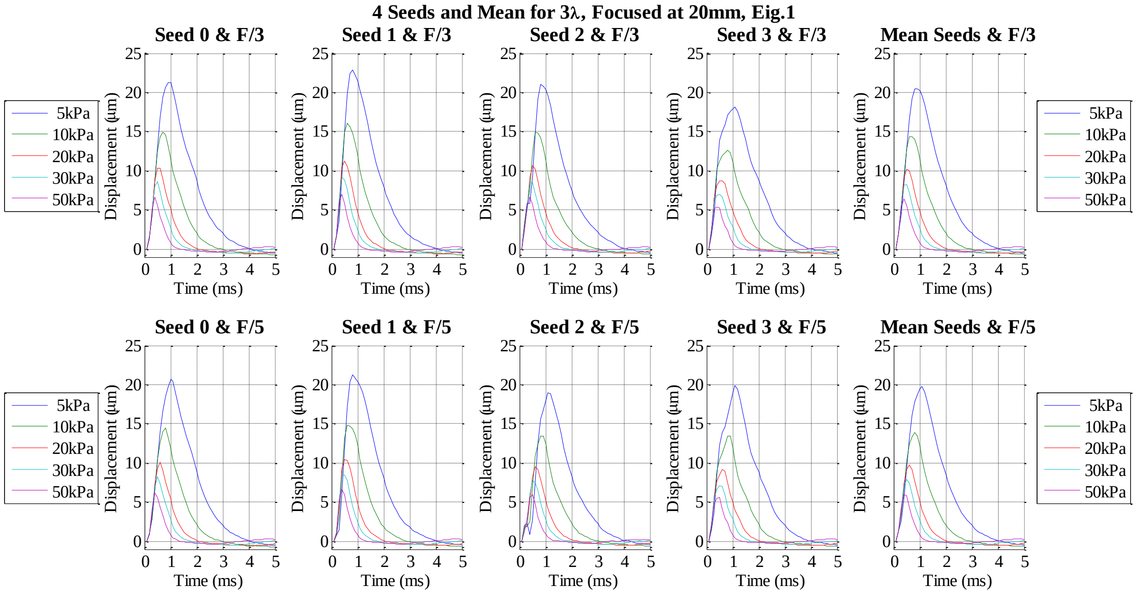
4 Seeds and Mean for 3λ, Focused at 20mm, Eig.1

Seed 0 & F/3 | Seed 1 & F/3 | Seed 2 & F/3 | Seed 3 & F/3 | Mean Seeds & F/3

Seed 0 & F/5 | Seed 1 & F/5 | Seed 2 & F/5 | Seed 3 & F/5 | Mean Seeds & F/5

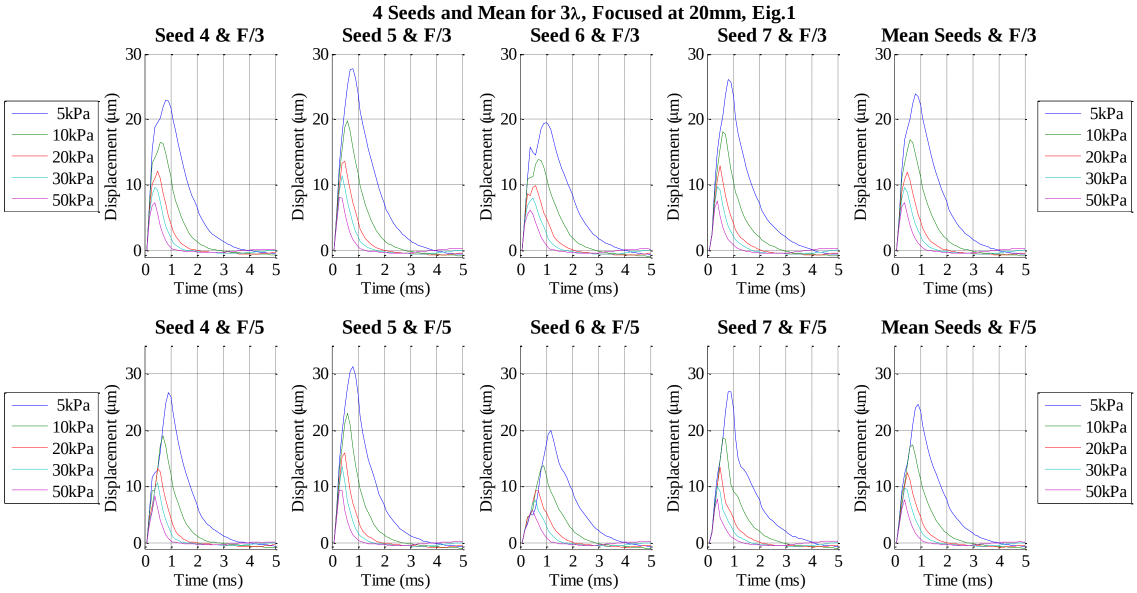
4 Seeds and Mean for 3λ, Focused at 20mm, Eig.1

Seed 4 & F/3 | Seed 5 & F/3 | Seed 6 & F/3 | Seed 7 & F/3 | Mean Seeds & F/3

Seed 4 & F/5 | Seed 5 & F/5 | Seed 6 & F/5 | Seed 7 & F/5 | Mean Seeds & F/5

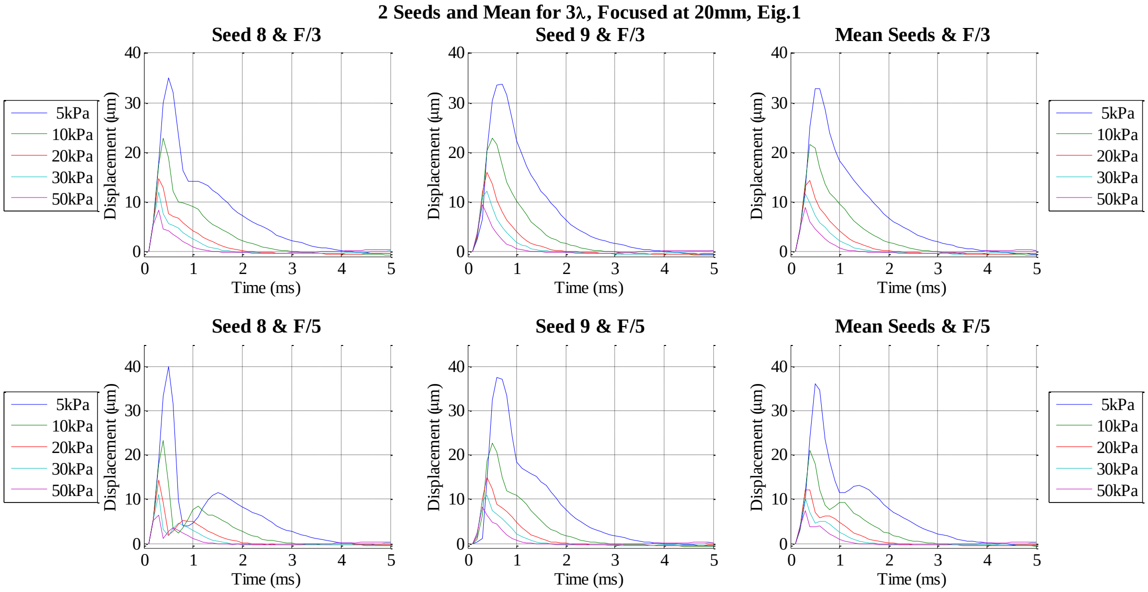

Time-to-Peak (TTP)

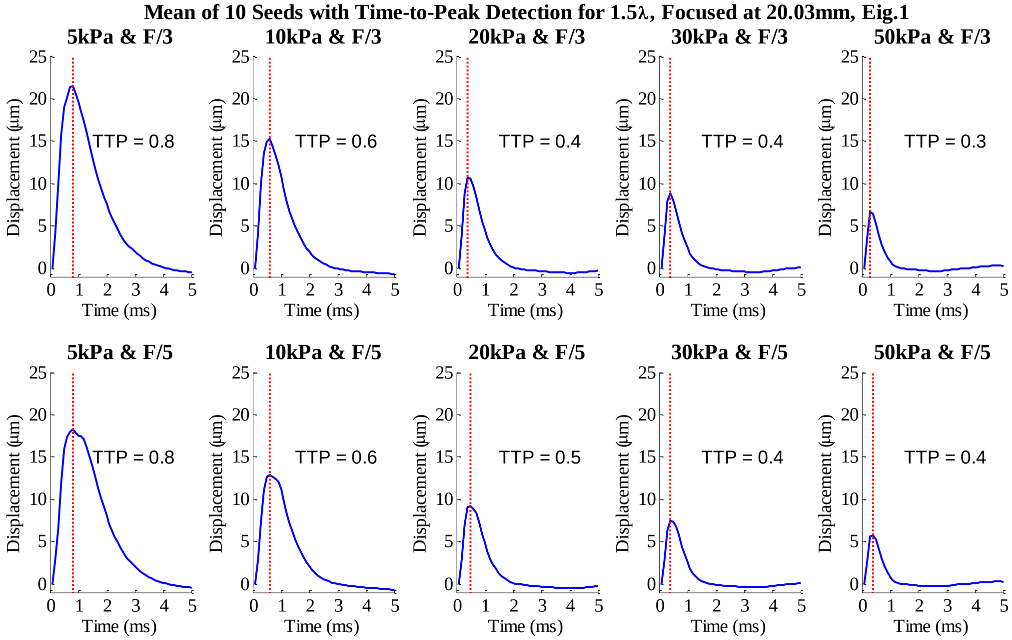

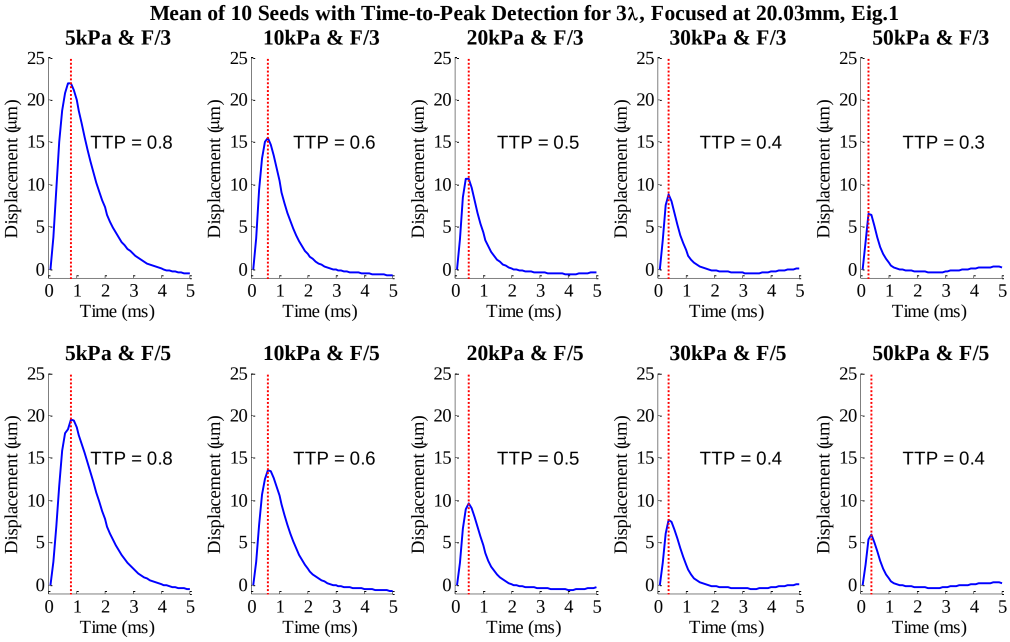
Mean of 10 Seeds with Time-to-Peak Detection for 3λ, Focused at 20.03mm, Eig.1

Time-to-Recovery (TTR)

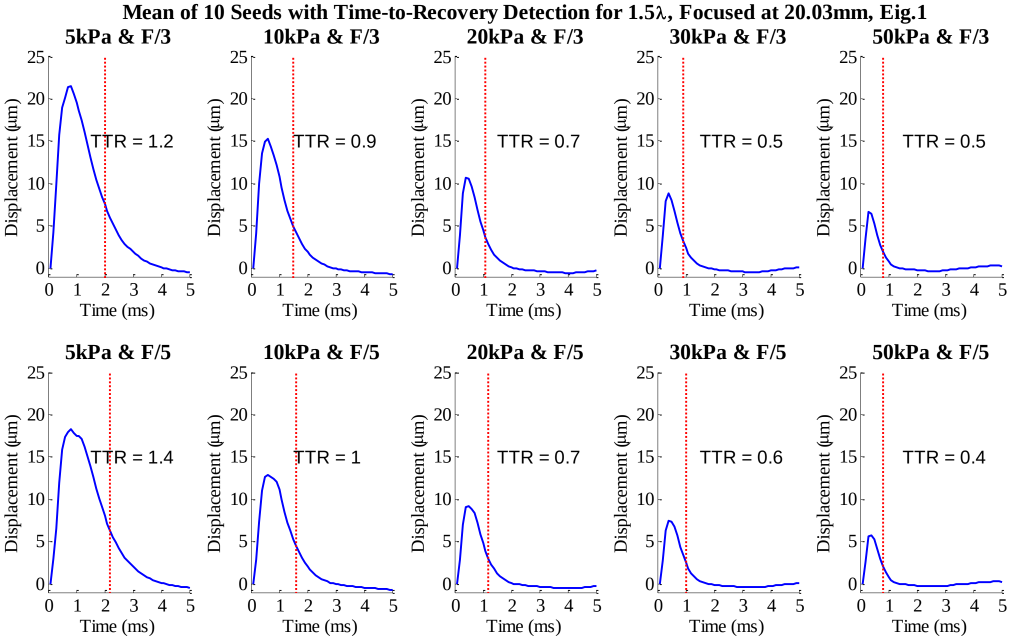
Mean of 10 Seeds with Time-to-Recovery Detection for 1.5λ, Focused at 20.03mm, Eig.1

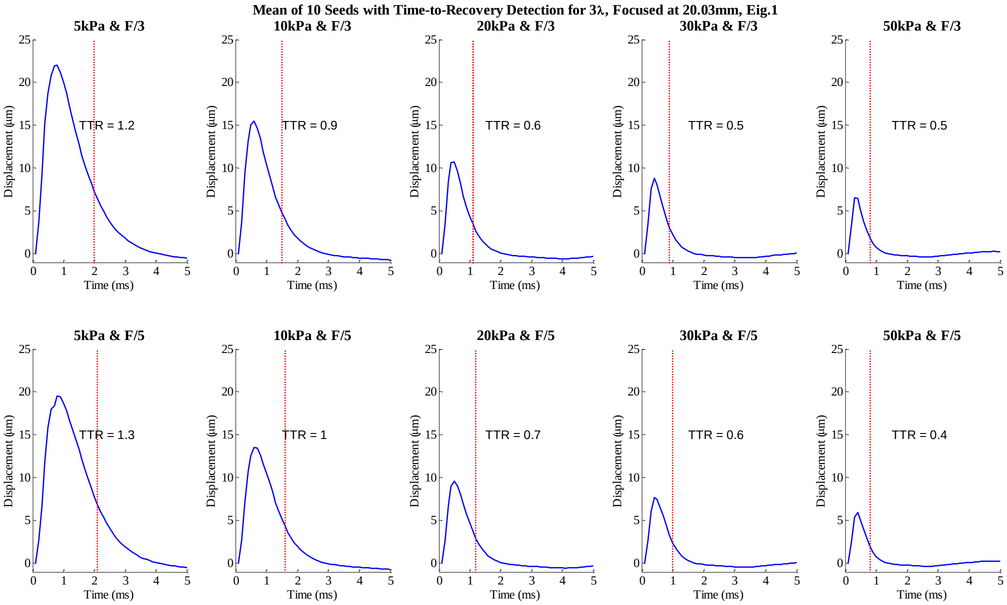
Mean of 10 Seeds with Time-to-Recovery Detection for 3λ, Focused at 20.03mm, Eig.1

5kPa & F/3

10kPa & F/3

20kPa & F/3

30kPa & F/3

50kPa & F/3

5kPa & F/5

10kPa & F/5

20kPa & F/5

30kPa & F/5

50kPa & F/5

REFERENCES

Doherty, J., Trahey, G., Nightingale, K., & Palmeri, M. (2013). Acoustic radiation force elasticity imaging in diagnostic ultrasound. *IEEE Transactions on Ultrasonics, Ferroelectrics, and Frequency Control*, *60*(4), 685–701. http://doi.org/10.1109/TUFFC.2013.2617

Fahey, B. J., Nightingale, K. R., Nelson, R. C., Palmeri, M. L., & Trahey, G. E. (2005). Acoustic radiation force impulse imaging of the abdomen: demonstration of feasibility and utility. *Ultrasound in Medicine & Biology*, *31*(9), 1185–98. http://doi.org/10.1016/j.ultrasmedbio.2005.05.004

Gallippi, C. M., Nightingale, K. R., & Trahey, G. E. (2003). BSS-based filtering of physiological and ARFI-induced tissue and blood motion. *Ultrasound in Medicine & Biology*, *29*(11), 1583–1592. http://doi.org/10.1016/j.ultrasmedbio.2003.07.002

Gallippi, C. M., & Trahey, G. E. (2003). Blind Source Separation-Based Velocity Estimation (BSSVE): Simulation and Clinical Results. In *IEEE Ultrasonics Symposium* (pp. 855–860).

Mauldin, F. W., Viola, F., & Walker, W. F. (2010). Complex principal components for robust motion estimation. *IEEE Transactions on Ultrasonics, Ferroelectrics, and Frequency Control*, *57*(11), 2437–2449. http://doi.org/10.1109/TUFFC.2010.1710

Mazza, E., Nava, A., Hahnloser, D., Jochum, W., & Bajka, M. (2007). The mechanical response of human liver and its relation to histology: an in vivo study. *Medical Image Analysis*, *11*(6), 663–72. http://doi.org/10.1016/j.media.2007.06.010

Nightingale, K. (2012). Acoustic Radiation Force Impulse (ARFI) Imaging: a Review. *Curr Medical Imaging*, *7*(4), 328–339. http://doi.org/10.2174/157340511798038657.Acoustic

Olympus Corporation. (n.d.). Ultrasonic Flaw Detection Tutorial. Retrieved January 1, 2015, from http://www.olympus-ims.com/en/ndt-tutorials/flaw-detection/

Palmeri, M. L., McAleavey, S. a., Trahey, G. E., & Nightingale, K. R. (2006). Ultrasonic tracking of acoustic radiation force-induced displacements in homogeneous media. *IEEE Transactions on Ultrasonics, Ferroelectrics, and Frequency Control*, *53*(7), 1300–1313. http://doi.org/10.1109/TUFFC.2006.1665078

Palmeri, M. L., Wang, M. H., Dahl, J. J., Frinkley, K. D., & Nightengale, K. R. (2009). Quantifying Hepatic Shear Modulus In Vivo Using Acoustic Radiation Force, *34*(4), 546–558.

Szabo, T. L. (2014). *Diagnostic Ultrasound Imaging: Inside Out*. *Diagnostic Ultrasound Imaging: Inside Out*. Elsevier. http://doi.org/10.1016/B978-0-12-396487-8.00003-3